Final Report
DOE Award Number DE-FG07-02ER63501

A Resolution Analysis of Two Geophysical Imaging Methods for Characterizing and Monitoring Hydrologic Conditions in the Vadose Zone

D. L. Alumbaugh
Formally with University of Wisconsin-Madison
Geological Engineering Program
Madison, WI 53706

D. J. La Brecque
Multi-Phase Technologies, LLC
Sparks, NV 89436

J. R. Brainard, Glenn Hammond
Sandia National Laboratories
P. O. Box 5800
Albuquerque, NM 87185-0819

Abstract

The objective of this research project was to analyze the resolution of two geophysical imaging techniques: electrical resistivity tomography (ERT) and cross-borehole ground penetrating radar (XBGPR) for monitoring subsurface flow and transport processes within the vadose zone. This was accomplished through a coupled approach involving very fine-scale unsaturated flow forward modeling, conversion of the resultant flow and solute fields to geophysical property models, forward geophysical modeling using the property model obtained from the last step to obtain synthetic geophysical data, and finally inversion of this synthetic data. These geophysical property models were then compared to those derived from the conversion of the hydrologic forward modeling to provide an understanding of the resolution and limitations of the geophysical techniques.

CONTENTS

1. Introduction and Project Objectives 10

2. STVZ Site OVERVIEW 12
   - 2.1 Instrumentation and Sensor Location 12
     - 2.1.1 Tensiometer, TDR, Solution Samplers, and Thermocouple Arrays 12
     - 2.1.2 ERT Electrode Arrays 12
     - 2.1.3 Sensor Data Acquisition Systems 14
     - 2.1.4 PVC-Cased Access Wells 14
   - 2.2 Site Geology 14
   - 2.3 Hydrologic Properties and Geophysical Property Measurements 17
     - 2.3.1 Background 17
     - 2.3.2 Hydraulic Property Measurements 17
   - 2.4 Infiltration System 18
   - 2.5 Timeline of Infiltration Events 18

3. Hydrological Modeling Background 21
   - 3.1 POR-SALSA 21
   - 3.2 Flow and Transport Simulations 21

4. Development of Hydrological Property Fields 23
   - 4.1 Layered Homogenous Property Fields 23
   - 4.2 Geostatistically-Correlated Property Fields 23
     - 4.2.1 Background 23
     - 4.2.2 Geostatistical Simulation Techniques 24

5. Flow and Transport Simulations 28
   - 5.1 Background 28
   - 5.2 Flow Simulations using Layered Homogeneous Property Fields 28
     - 5.2.1 Six Layer Simulations 28
     - 5.2.2 Twenty-nine Layer Simulations 30
   - 5.3 Flow Simulations using Geostatistically Correlated Property Fields 33
     - 5.3.1 Six-layer Simulations 33
     - 5.3.2 One-Layer Simulations 35
   - 5.4 Transport Simulations 37

6. Analysis of ERT Inversion 39
   - 6.1 Introduction 39
   - 6.2 Improvements to ERT Modeling 40
     - 6.2.1 Calculation of Resistivity From Hydrological Models 40
     - 6.2.2 Forward Modeling Considerations 40
   - 6.3 Modeling of Synthetic Hydrological Data 43
   - 6.4 Comparison of Synthetic Models 43
   - 6.5 Comparison of Models and Quantification of Improvements 48
   - 6.6 Conclusions 49

7. Cross-Borehole Ground Penetrating Radar 52
   - 7.1 Electromagnetic FDTD Forward Modeling 52
     - 7.1.1 Finite Difference Solutions for Radar Wave Propagation 52

7.1.2 Model Design for FDTD EM Forward Modeling 53
7.2 GPR Tomographic Inversion Algorithm 55
7.3 Potable Water Infiltration Flow Simulations 56
7.4 Transport Simulations 62
7.5 Conclusions 63
8. References 66

FIGURES

Figure 2-1. Plan-view schematic of the instrumentation layout at the STVZ. 13
Figure 2-2. Detailed stratigraphic column obtained from the NW core from the STVZ. 15
Figure 2-4. Timeline of infiltration events at the STVZ showing the extended period of potable water infiltration between Day 0 and Day 800 followed by the first and second salt pulses, each followed by a short period of potable water flush. 19
Figure 5-1. Two dimensional slice showing the moisture content distributions for the 6-layer homogeneous case. 29
Figure 5-2. Plots of simulated (left) and measured (right) moisture saturation profiles. The measured data is derived from neutron moisture meter readings in the center access tube at the STVZ. 30
Figure 5-3. Two-dimensional slice showing the moisture distribution from the 29-layer simulation at Day 0 and Day 40. 32
Figure 5-4. Comparison between the simulated moisture content profiles at Day 0 and Day 80 and that measured at the STVZ at Day 40 from the center access tube 32
Figure 5-5. Two-dimensional slice showing the moisture distribution from the six-layer heterogeneous case. 34
Figure 5-6. Comparison between the simulated moisture content profiles at day zero and 80 and that measured at the STVZ at comparable days from the center access tube. 35
Figure 6-1. Finite-difference forward model error relative to the analytic result for a 100 ohm-m half space for trials of (a) background to foreground ratios and (b) pad element elongation ratio. 42
Figure 6-2. Semi-variogram of background synthetic model showing results over 6 meters for the uncompressed 6.25 cm model, the compressed 37.5 cm model and inversion results on the 37.5 cm mesh for the ultimate (new) method, the improved method with better padding and a mesh based on that used for the original STVZ field study. 44
Figure 6-3. Visual comparison of Day 20 synthetic infiltrations showing (a) 6.25 cm hydrological model converted to conductivity, (b) ultimate, new inversion method, (c) STVA field – style mesh, (d) old inversion method with improved pad scheme. 45
Figure 6-4. Visual comparison of Day 361 synthetic infiltrations showing (a) STV field – style mesh (b) ultimate, new inversion method. 45
Figure 6-5. (a) High resolution 6.25 cm model; (b) and (d) 37.5 cm compression of model in (a); the image in (c) shows the result of the new inversion method for 181 days. 46
Figure 6-6. Transport models showing (a) inverted result and (b) inverted model at Day 20; and (c) inverted result and (d) synthetic model at Day 50. 47

Figure 6-7. Difference inversion of synthetic transport model at Day 50 showing (a) new inversion result and (b) 37.5 cm compressed synthetic model. 48
Figure 6-8. Original inversion of STVZ Phase II transport data showing (a) 10/01/01 raw result (b) 10/01/01 temperature corrected result, (c) 01/31/02 raw result and (d) 01/31/02 temperature corrected result. 49
Figure 6-9. Comparison of original and ultimate (new) inversions of STVZ Phase II transport data showing (a) 10/01/01 ultimate temperature corrected result, (b) 01/31/02 ultimate temperature corrected result.. 50
Figure 7-1. Pre-infiltration water content field. The rectangle encloses the area of study...... 57
Figure 7-2. Images of water content at time = Day 0 as estimated from the XBGPR velocity images. (a) The input field, or true model, and (b) the results estimated from the travel-time generated velocity image.. 58
Figure 7-3. Images of water content at Day 10 after the beginning of the fresh-water infiltration. (a) The true model total moisture content field. (b) The inversion results in terms of total moisture content. (c) The true-model change in moisture content relative to Figure 7-2a. (d) The inverted change in moisture content relative to Figure 7.2b. 58
Figure 7-4. Images of water content at Day 30 after the beginning of the fresh-water infiltration. (a) The true model total moisture content field. (b) The inversion results in terms of total moisture content. (c) The true-model change in moisture content relative to Figure 7-2a. (d) The inverted change in moisture content relative to Figure 7.2b. 59
Figure 7-5. Images of water content at 60 days after the beginning of the fresh-water infiltration. (a) The true model total moisture content field. (b) The inversion results in terms of total moisture content. (c) The true-model change in moisture content relative to Figure 7-2a. (d) The inverted change in moisture content relative to Figure 7.2b. 59
Figure 7-6. Pre-infiltration attenuation field. (a) The input field, or true model, and (b) the results estimated from the attenuation imaging. 60
Figure 7-7. Images of attenuation at Day 10 after the beginning of the fresh-water infiltration. (a) The true model attenuation field. (b) The inversion results in terms of attenuation. (c) The true-model change in attenuation relative to Figure 7-6a. (d) The inverted change in attenuation relative to Figure 7.6b. 61
Figure 7-8. Images of attenuation at Day 30 after the beginning of the fresh-water infiltration. (a) The true model attenuation field. (b) The inversion results in terms of attenuation. (c) The true-model change in attenuation relative to Figure 7-6a. (d) The inverted change in attenuation relative to Figure 7.6b. 61
Figure 7-9. Images of attenuation at Day 60 after the beginning of the fresh-water infiltration. (a) The true model attenuation field. (b) The inversion results in terms of attenuation. (c) The true-model change in attenuation relative to Figure 7-6a. (d) The inverted change in attenuation relative to Figure 7.6b. 62
Figure 7-10. Attenuation for 1000ppm transport at time = Day 30. (a) The input attenuation field or ‘true model’. (b) The results from processing and inverting the synthesized amplitude data for attenuation... 63

Figure 7-11. Attenuation for 6900ppm transport at time = Day 30. (a) The input attenuation field or 'true model'. (b) The results from processing and inverting the synthesized amplitude data for attenuation. 64

TABLES

Table 5-2. Hydraulic properties used in the 29 layer flow simulations. 30

NOMENCLATURE

CO_2	carbon dioxide
dB	decibel
DOE	Department of Energy
EM	Electromagnetic
ERT	electrical resistivity tomography
FD	finite-difference
MDC	main drainage curve
MOG’s	Multi-Offset Gathers
MWC	Main wetting curve
Np	neper
PDCs	Primary drainage curves
pdf	probability density functions
SE	southeast
SIRT	simultaneous iterative reconstruction technique
SNL	Sandia National Laboratories
STVZ	Sandia-Tech Vadose Zone experimental facility
SW	southwest
TD	time-domain
TDR	time-domain reflectometry
TE	transverse electric
TM	transverse magnetic
VEAs	vertical electrode arrays
XBGPR	cross-borehole ground penetrating radar

EXECUTIVE SUMMARY

The objective of this research project was to analyze the resolution of two geophysical imaging techniques: electrical resistivity tomography (ERT) and cross-borehole ground penetrating radar (XBGPR) for monitoring subsurface flow and transport processes within the vadose zone. This was accomplished through a coupled approach involving very fine-scale unsaturated flow forward modeling, conversion of the resultant flow and solute fields to geophysical property models, forward geophysical modeling using the property model obtained from the last step to obtain synthetic geophysical data, and finally inversion of this synthetic data. These geophysical property models were then compared to those derived from the conversion of the hydrologic forward modeling to provide an understanding of the resolution and limitations of the geophysical techniques.

Hydrologic models and the properties used in this project were based on a constant flux infiltration experiment and subsequent tracer experiments performed at the Sandia-Tech Vadose Zone Facility (STVZ) near Socorro, New Mexico as part of an earlier EMSP (Project #55332). Hydrologic property data necessary for the unsaturated flow modeling, and geophysical properties necessary for the conversion of the moisture content field to resistivity came from measurements made on samples collected from the STVZ. The models were ran on a supercomputer platform at Sandia National Laboratories with POR-SALSA, which is a two-phase, three dimensional finite-element code designed to run on massively parallel computers. These models were carried out with 25, 12.5 and 6.35 grid discretizations within a 1728 m^3 region. Simulations incorporated property fields comprised of one and six homogeneous layers and more complicated, geostatistically-correlated property fields.

Comparisons between simulated and field measured data indicate that the simulated flow fields consistently overestimated the change in moisture contents from pre to final infiltration as well as the final moisture content. Steps to resolve these discrepancies included 1) developing a detailed 29 layer model with hydraulic property fields derived by combining in-situ measurements at the STVZ and the property measurements from samples and 2) performing a comprehensive parameter study where parameters used in the equations that describe the unsaturated hydraulic properties were systematically varied from one simulation to the next. Both of these efforts resulted in better agreement between the simulated results and simulated data, but failed to reproduce the measured data with great accuracy.

The geophysical analyses presented in this report used results from high resolution (6.25 cm grid discretization) hydrological simulation that incorporated properties selected from the series of lower resolution simulations (25 cm grid discretization) which were performed for the parameter study mentioned above. For the ERT study, the three-dimensional moisture content fields from the high resolution hydrological simulation (synthetic fields xxxx were converted to resistivity fields. These resistivity fields were then used to forward model the electrical field in a domain duplicating the ERT electrode placement at the STVZ. Inversion of the ERT forward modeling results were then compared to the original resistivity fields to establish the measurement resolution capability of ERT. At the STVZ, the vertical ERT electrode spacing was 75 cm. Several improvements in the in the ERT forward modeling and inversion process resulted in better agreements between the hydrological derived resistivity fields and those from the ERT inversion process. Additionally application of temperature corrections to the inverted data also improved agreement between the two data sets.

As a result of these studies, it was determined that ERT is able to resolve 3D character (location of highs and lows of the hydrological data match the highs and lows of the inverted data), and scale (extent of wetting front very similar to that measured in the field) of the hydrological and tracer data. Some reduction in character is apparent in that the contrasts between the highs and lows are somewhat subdued. However, bulk conductivity changes from pre infiltration/tracer to post infiltration/tracer conditions appear to be accurately represented in terms of both location and intensity.

With XBGPR, the first-arrival time (travel time) and amplitude of the received EM signals are used to invert for velocity and attenuation. Petrophysical conversion provides two-dimensional distributions of moisture content and solute concentration. With velocity data, comparison of moisture content distributions between hydrological and inverted data shows that the inversion causes a loss of detail in that highs and lows are somewhat subdued in the inverted images. In addition, moisture content differences between the pre- and post-infiltration images show artifacts not present in the true models. However, the inversions of the absolute moisture content seems to always reproduce the general character of the hydrological data (location of highs and lows of the hydrological data match the highs and lows of the inverted data), and both the absolute and differenced images reproduce the scale (extent of wetting front very similar to that measured in the field) quite well.

The attenuation images provide a reasonable idea of the extent of the flow plume. However, severe artifacts are present in all the images. This could be due to the straight ray assumption and other violations of the underlying physics that are present within the processing and inversion. With the addition of salt water to the system, the magnitude of the attenuation increased enough that the images are much better than those reconstructed from the potable water simulations. Again, the overall character of the flow is well constrained and larger details of the heterogeneous structure are apparent. The input fields and inverted images have similar scales. When the input concentration was increased from 1000 ppm to 6900 ppm, the depth of transport was clearly imaged in the early time steps. However, when the attenuation exceeded 6 Np/m, most of the signal was lost resulting in a near total loss of resolution at later times.

1. INTRODUCTION AND PROJECT OBJECTIVES

Geophysical methods are rapidly becoming important within the Department of Energy (DOE) complex as tools for characterizing subsurface hydrologic properties, as well as monitoring flow and transport processes within the vadose zone at contaminated sites. The reason for incorporating geophysical imaging into site characterization, remediation monitoring, or as a long-term monitoring tool for a site closure plan is simple; these methods offer the possibility to non-destructively characterize subsurface conditions and processes from a limited number of boreholes and/or measurements made on the surface.

To convert between geophysical and hydrological properties requires the application of petrophysical models. In general, petrophysical models are approximate, empirical relations developed from studies of core-sized (dimension of a few cm) samples. However, geophysical images typically have resolutions on the order of fractions of meters or larger. In the past, there has been little work done to quantify the effect of heterogeneity due to structures that are larger than core samples but still too small to be resolved individually by geophysical imaging. In addition, there has been little work done to quantify the resolution of the imaging schemes that addresses their ability to characterize spatial heterogeneity within the vadose zone, and produce accurate time-lapse images of flow and transport processes.

The effects of data error on the images such as sensor mispositioning and incorrect calibration are generally unknown. Thus, in performing this work, it is important to consider the cumulative effect of errors in both the geophysical data collection and processing, and within petrophysical models themselves, if interpreters are to understand those features in the images that are real, those that are artifacts, and how much credence can be given to the results in terms accuracy and precision.

This report details efforts aimed at resolving some of these issues for the electrical resistivity tomography (ERT) and cross-borehole ground penetrating radar (XBGPR) geophysical methods as applied to characterizing and monitoring vadose zone properties and processes. This research consisted of four primary tasks:

1) high-definition, large-scale numerical modeling of a series of statistically related vadose zone flow and transport processes to yield porosity, moisture content, and solute concentrations at 25.0, 12.5 and 6.25 cm intervals throughout a 1700 m^3 volume vadose zone based on hydrologic properties and boundary conditions during infiltration and tracer tests performed at the Sandia-Tech Vadose Zone experimental facility (STVZ) located in Socorro, New Mexico;

2) application and analysis of petrophysical relationships that convert the output of the hydrologic models from task 1 into geophysical parameter fields: resistivity for the ERT method, the dielectric and electrical conductivity for XBGPR.

3) generation of synthetic ERT and XBGPR data sets from the geophysical parameter fields generated in task 2 through forward modeling within domains that duplicated the ERT electrode placement and XBGPR transmitter and receiver locations at the STVZ.

4) imaging of the synthetic data sets using standard geophysical processing and inversion techniques, and comparison of the results to the original hydrologic models.

During an early phase of the project, infiltration and solute transport experiments were performed at the Sandia-Tech Vadose Zone (STVZ) site. For this phase of the project, hydrological flow simulations were carried out at the Sandia National Laboratory (SNL) supercomputing facilities using the POR-SALSA hydrological modeling code and the STVZ experiments as a template. The approach was to mimic the heterogeneous, stochastic nature of the site rather than trying to duplicate the precise flow field at the STVZ.

Two geophysical techniques were applied to the simulated hydrological results, ERT and XBGPR. For the ERT portion of the project, synthetic ERT data were created by converting simulated moisture content fields from the high-resolution flow simulations to electrical resistivity. The resistivity data was then used in a forward model of ERT generated electrical field within a domain that duplicated electrode placement at the STVZ. The resultant ERT data were then modeled using fine-scale, high-resolution meshes and inverted using coarse meshes similar to those that were used for normal inversion of field data. The goal was to demonstrate the ability of ERT to resolve the hydrological models and to identify improvements in technique that would improve resolution.

With XBGPR, the first-arrival time (travel time) and amplitude of the received EM signals are used to invert for velocity and attenuation. Petrophysical conversion provides two-dimensional distributions of moisture content and solute concentration. With velocity data, comparison of moisture content distributions between hydrological and inverted data shows that the inversion causes a loss of detail in that highs and lows are somewhat subdued in the inverted images. In addition, moisture content differences between the pre- and post-infiltration images show artifacts not present in the true models. However, the inversions of the absolute moisture content seems to always reproduce the general character of the hydrological data (location of highs and lows of the hydrological data match the highs and lows of the inverted data), and both the absolute and differenced images reproduce the scale (extent of wetting front very similar to that measured in the field) quite well.

The attenuation images provide a reasonable idea of the extent of the flow plume. However, severe artifacts are present in all the images. This could be due to the straight ray assumption and other violations of the underlying physics that are present within the processing and inversion. With the addition of salt water to the system, the magnitude of the attenuation increased enough that the images are much better than those reconstructed from the potable water simulations. Again, the overall character of the flow is well constrained and larger details of the heterogeneous structure are apparent. The input fields and inverted images have similar scales. When the input concentration was increased from 1000 ppm to 6900 ppm, the depth of transport was clearly imaged in the early time steps. However, when the attenuation exceeded 6 Np/m, most of the signal was lost resulting in a near total loss of resolution at late times.

2. STVZ SITE OVERVIEW

A brief overview of the Sandia-Tech Vadose Zone Facility is given to provide the background for the discussions on both the hydrological and geophysical modeling undertaken as part of this project.

2.1 Instrumentation and Sensor Location

The STVZ is instrumented with arrays of transducer-equipped tensiometers, solution samplers, time-domain reflectometry (TDR) probes, thermocouples, and ERT electrode arrays. PVC pipes measuring 2 in. in diameter provide access for down-hole geophysical measurements. All arrays are arranged in an axisymmetric pattern as seen in plan view and cover a 10-by-10-m area. The arrays are centered on the 3-by 3-meter infiltrometer. Instrument locations and identifiers are given in Figure 2-1, and the subsurface arrays are discussed below. Sensor specifications, sensor-calibration procedures and results, installation geometry, installation coordinates, and data acquisition system descriptions for all sensors are given in Brainard et al., (2005). Brief descriptions follow here.

2.1.1 Tensiometer, TDR, Solution Samplers, and Thermocouple Arrays

A total of 88 pressure-transducer–equipped tensiometers were installed at the site in three separate arrays. The arrays include 16 tensiometers installed in nests of two in the infiltrometer (infiltrometer tensiometers), 64 tensiometers installed in nests of four and in groups of four on each side of the infiltrometer (T4 tensiometers), and 8 tensiometers installed in nests of two near each corner of the infiltrometer (T2 tensiometers). The infiltrometer tensiometers are installed in each of the outside infiltration arrays. A description of the infiltration arrays is provided in Section 2.4. The porous cups of these tensiometers are located 0.5 and 1 m below the infiltration surface. Target depths for the T2 tensiometers were 3 and 6 m below the ground surface, while the target depths for the T4 tensiometers were 2, 4, 6, and 8 m. Actual depths were measured relative to a datum with a theodolite and a surveying rod. Most tensiometers were installed within a few centimeters of the target depths.

Installed just below the porous cups of each of the T2 tensiometers and the deepest T4 tensiometers (8 m) is a solution sampler followed by a TDR probe. This arrangement yields 24 solution samplers and 24 TDR probes.

A thermocouple is attached near the porous cups of each of the T4 tensiometers in two diagonally opposite nests in each quadrant. Thus, subsurface temperatures are monitored at depths close to 2, 4, 6, and 8 m below the ground surface within two nests in each quadrant.

2.1.2 ERT Electrode Arrays

Two types of ERT arrays are installed at the site: vertical electrode arrays (VEAs) and surface arrays (see Figure 2-1 for installation locations of both array types). Eight VEAs are installed at the site, each array extending to approximately 13 m below the surface. Each array has 17 equally spaced electrodes at 0.75-m intervals. Four VEAs are placed 3.75 m from the center of the infiltrometer (inner VEAs) in each of the principal directions. The other four VEAs are located about 7.4 m from the center of the infiltrometer (outer VEAs) and are located at 45° to the principal compass directions.

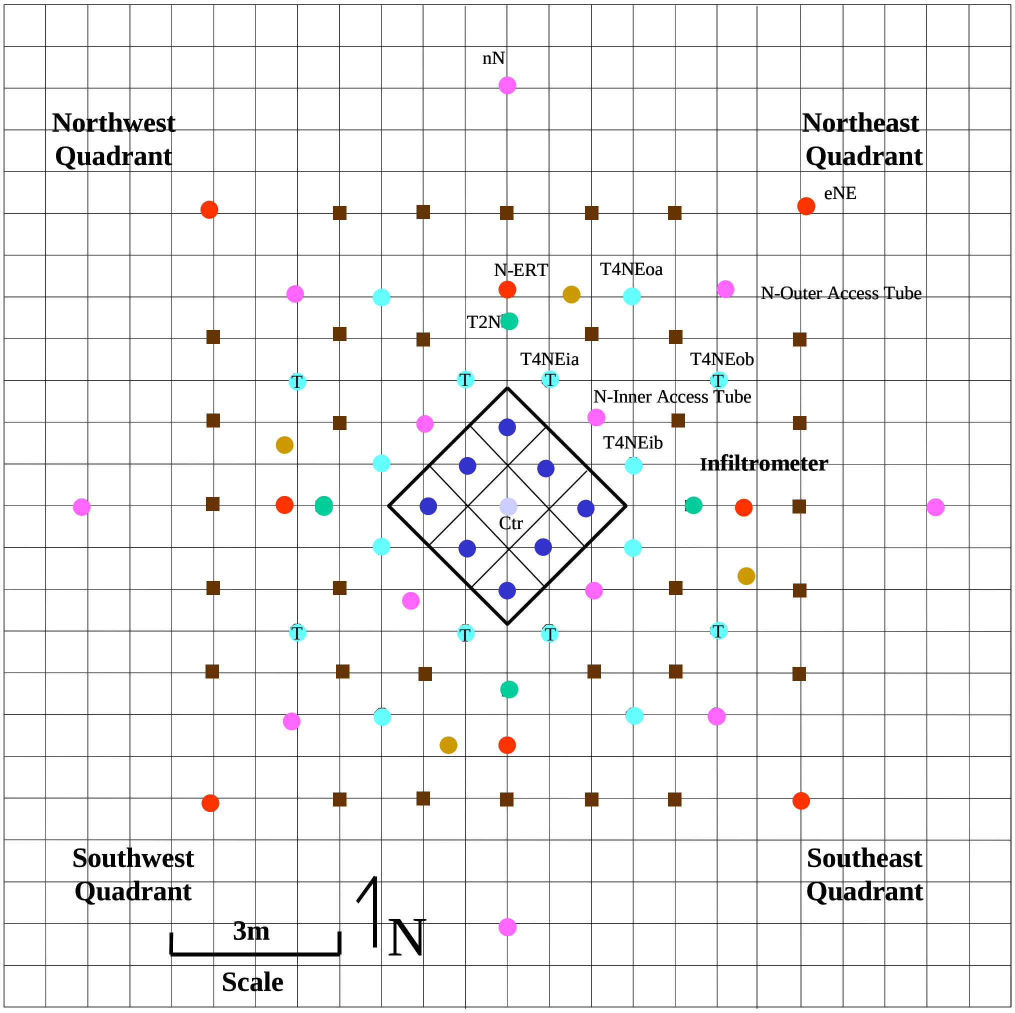

The nomenclature for identifying instrument and access tube locations is given for the NE array. Location identifiers for the other arrays are obtained by rotating the NE quadrant array 90 degrees about the center access tube and changing the quadrant abbreviation to specify the new quadrant.

- ● Four-Nested Tensiometer Locations (T4 ID prefix). The tensiometer porous cups are approximately 2, 4, 6, and 8 meters below the ground surface/datum. A TDR probe is installed at the bottom of each hole with a suction lysimeter immediately above. The TDR probe/suction lysimeter pair is located just below deepest tensiometer porous cup. T T4 nests where thermocouples are installed within 10 cm of each tensiometer porous cup.
- ● Two-Nested Tensiometer Locations (T2 prefix). Each hole has two instrument clusters consisting of a tensiometer, a suction lysimeter, and a TDR probe (listed from top to bottom). The clusters are approximately 3.5 and 6 meters below the ground surface/datum.
- ● Infiltrometer Tensiometers. The tensiometer porous cups are installed approximately 0.5 and 1 meter below the surface
- ● PVC Cased Wells (n prefix). Used for collecting neutron, GPR data, electrical conductivity and gamma data.
- ● ERT electrode string (e Prefix) ■ ERT surface electrode ● Continuous Core Sample Locations

Figure 2-1. Plan-view schematic of the instrumentation layout at the STVZ.

A total of 36 surface ERT electrodes were installed at the site. Five surface electrodes were installed in a line between each pair of outer VEAs for a total of 20, 3 were installed in between 3 of the 4 T4 tensiometers in each quadrant for a total of 12 surface electrodes, and 4 were installed in the infiltrometer.

2.1.3 Sensor Data Acquisition Systems

All of the subsurface-sensor data acquisition systems are described in detail in Brainard et al., (2005). Brief descriptions are given below.

The thermocouple and tensiometer data acquisition systems are composed of Campbell Scientific 21X dataloggers and 16-port multiplexers. The ERT system consists of the following five components:

1. A central computer with a serial port, modem, and high-speed GPIB data bus
2. A receiver consisting of four fully isolated voltmeters for receiving signals
3. A transmitter/controller unit for controlling the output waveform and triggering the voltmeters
4. An external power supply providing high-voltage direct current
5. A group of four multiplexers that allow the transmitter and receiver to be connected to any combination of electrodes

The TDR system consists of the following three components:

1. A central computer
2. A Tektronix 1502b signal generator
3. A 24-port JVW radio-frequency multiplexer

2.1.4 PVC-Cased Access Wells

Thirteen 2-in.-diameter PVC tubes were installed within the instrumented area to depths of 12.5 to 13 m to provide access for cross-well radar logging and down-hole logging. Twelve of the PVC tubes are arranged in three rings around the center of the infiltrometer, with the 13th tube located in the center of the infiltrometer (see Figure 2-1). In the outer ring, the tubes are located 7.5 m away from the center of the infiltrometer in each of the four compass directions. In the next two rings, the tubes are rotated 45° from the outer ring and relative to the center of the infiltrometer. The inner and middle rings are located 2.2 m and 5 m, respectively, from the center of the infiltrometer.

Down-hole logging measurements include neutron thermalization, induction logging for electrical conductivity, and natural gamma. In addition, a XBGPR study was conducted along a straight-line transect of five access tubes.

2.2 Site Geology

The sediments at the STVZ are mapped as part of the Sierra Ladrones Formation (Pliocene to Pleistocene) of the Upper Santa Fe Group, a basin-fill deposit within the Rio Grande Rift (Hawley, 1983). At the STVZ, this formation consists mostly of interbedded sands and gravels showing internal structure common to fluvial sediments (complex sets of cross-beds, for example). A medium- to thick-bedded gravelly clay bed and very thinly bedded silty-to-sandy clay beds make up a small, but important, component of the stratigraphy at the STVZ.

The stratigraphy at the STVZ was revealed from several sources of information. Four continuous-core samples, taken to a depth of 12 m (see Figure 2-1 for locations), were used to develop four detailed stratigraphic columns, one of which is presented in Figure 2-2 (see

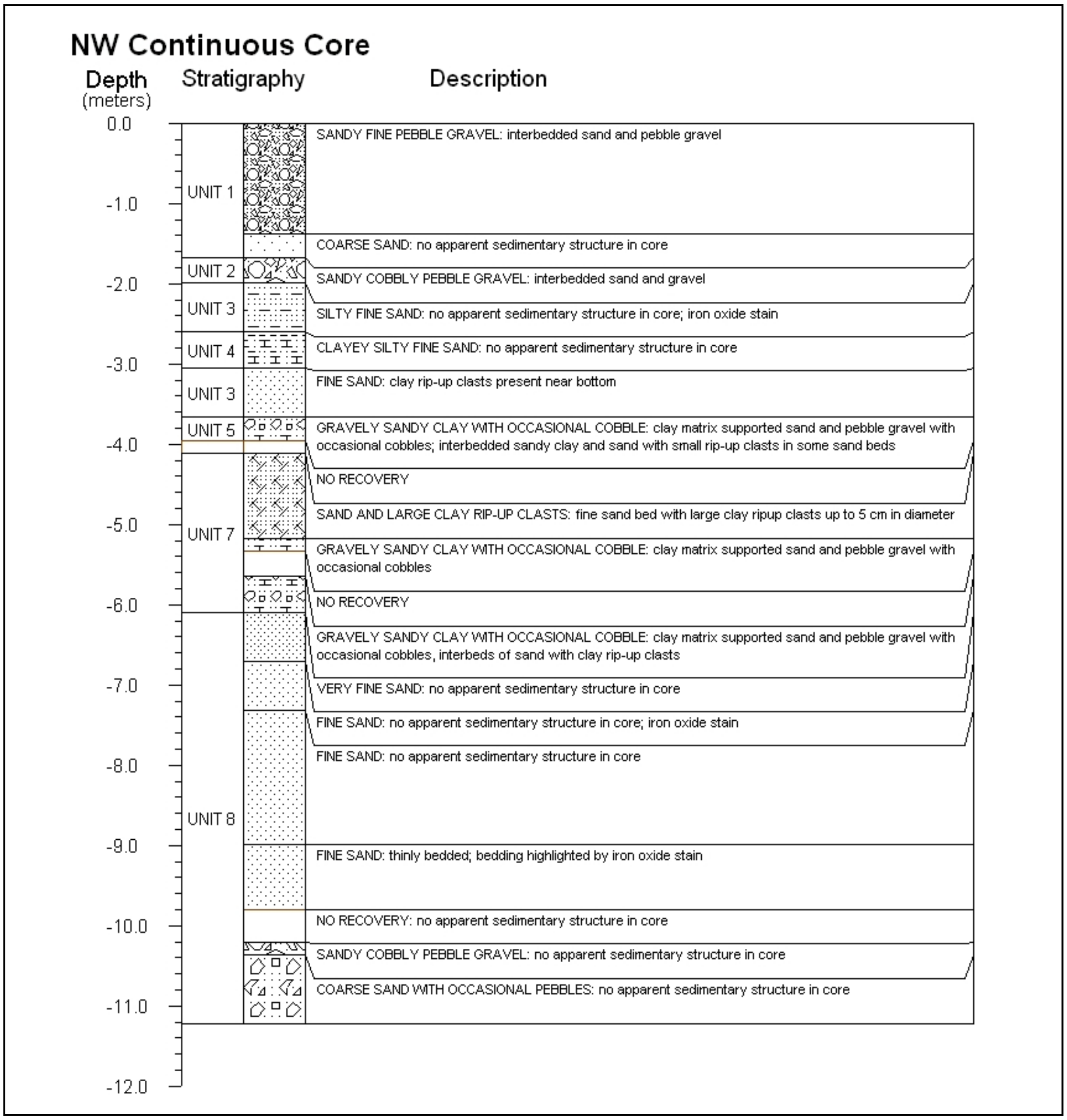

Figure 2-2. Detailed stratigraphic column obtained from the NW core from the STVZ.

Brainard et al. 2005 for more detail). These detailed stratigraphic columns provided the basis for identifying geologic units, while cuttings from all of the 41 instrumentation boreholes, varying in depth from 12 to 18 m, and geologic well logs, electrical-inductance borehole logs, and natural-gamma borehole logs aided in correlating the units identified within the stratigraphic columns and extending the units to the instrumentation wells. Figure 2-3 illustrates a generalization of the stratigraphy and assumed correlations between units based on Figure 2-2 and the three other stratigraphic columns presented in Brainard et al. (2005).

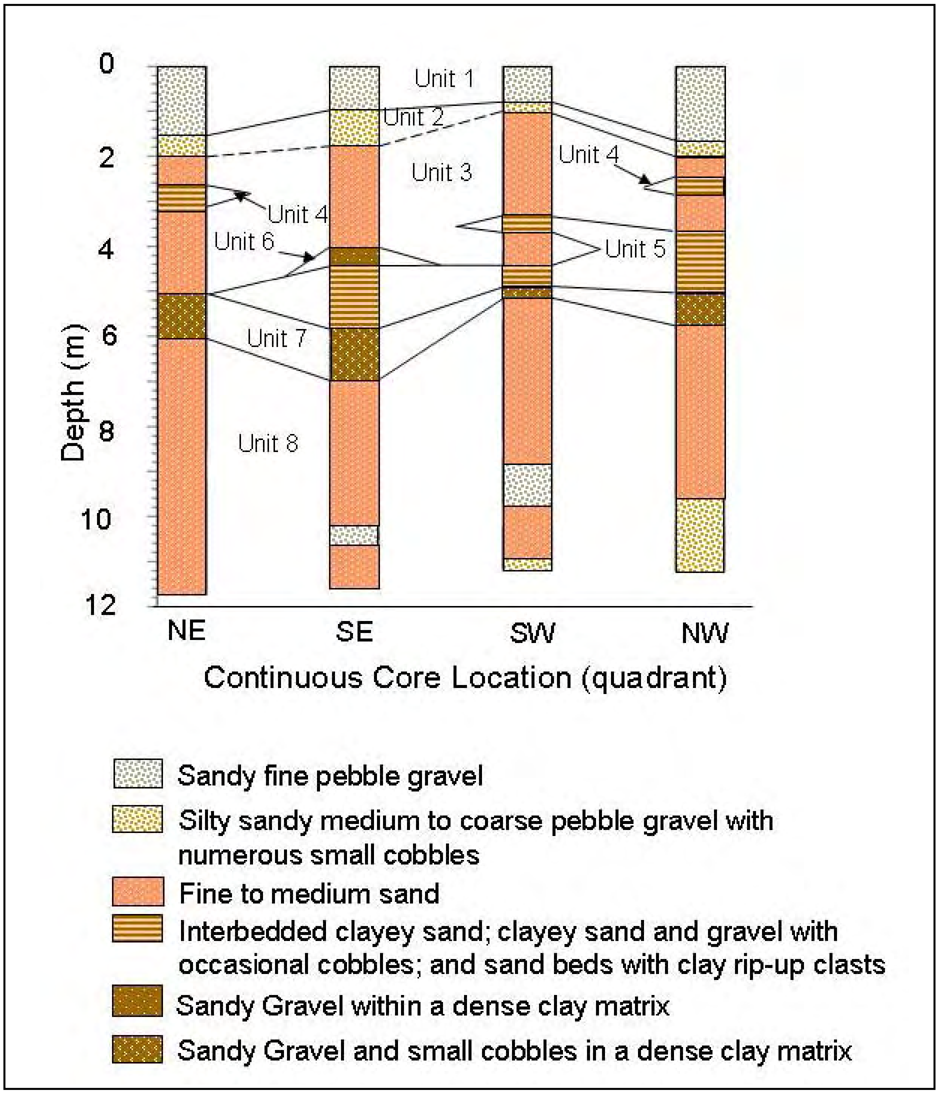

Figure 2-3: Generalized interpretation of the four detailed descriptions of the stratigraphy at the STVZ derived from continuous core samples.

A generalized description of the stratigraphy presented in Figures 2-2 and 2-3 is given next. Two sandy gravel beds form the units closest to the surface, Unit 1 and Unit 2, respectively, attaining a thickness of 2 m. A sharp increase in silt, fine sand, and cobbles in the lower bed distinguishes the two beds. The difficulty experienced at all the well sites while drilling through Unit 2 attests to a consistent presence of this cobble bed across the site. Below the lower gravel bed is a thick sand bed (Unit 3) intervened by a clay-rich bed near a depth of 3 m (Unit 4) in the NW and NE continuous-core sample locations and another near 4 m in the southwest (SW) continuous-core sample. The absence of a clay bed at these depths in the southeast (SE) core, as well as minimal recovery in drilling cuttings of this unit in some other areas, attests to the thinning and pinching out of these clay beds. In contrast, the lowest clay bed (Unit 5), which is between 5 and 7 m, appears to be continuous across the site. In particular, the lowest clay bed consistently shows as sandy gravel with small cobbles supported by a dense clay matrix. Below the last clay bed is a very thick sand deposit containing occasional intervening gravel lenses as well as a sandy gravel deposit (Unit 6) extending beyond the bottom of the NE and SW boreholes**.**

2.3 Hydrologic Properties and Geophysical Property Measurements

2.3.1 Background

Both inverse and forward numerical codes rely on parametric equations to reproduce measured moisture-retention curves, i.e., moisture content versus tension head. One such equation is the relationship described by van Genuchten (1980), further referred to as the VG equation:

$$\theta = (\theta_s - \theta_r)\left[1 + (\alpha h)^n\right]^{-m} + \theta_r \, . \tag{2-1}$$

where θ_s is the satiated volumetric moisture content, θ_r is the residual moisture content, α is a curve-fitting parameter [cm^{-1}] with $1/\alpha$ [cm] signifying the air-entry pressure, n and m are also curve-fitting parameters with n being related to the pore-size distribution of the porous media and which impacts the slope of $\theta(h)$. Both n and m are dimensionless. Commonly, m is taken as $1-1/n$. Finally, h [cm] is the tension head.

These parametric equations are commonly used in conjunction with theoretical pore-size distribution models such as those developed by Mualem (1976) and Burdine (1953) to predict the unsaturated hydraulic conductivity. These models require that the saturated hydraulic conductivity K_s be known.

At the STVZ, the “unsaturated hydraulic properties,” e.g., $\theta_r, \theta_s, \alpha, n$, in Equation 2-1 as well as K_s were obtained through laboratory measurements. These measurements are briefly discussed next while Brainard et al., (2005) and Baker (2001) contain a complete description of the measurement procedures and results.

2.3.2 Hydraulic Property Measurements

Due to the unconsolidated nature of the core, intact samples could not be collected. Instead, samples were collected from homogenized 0.15 m sections of a 11 m deep continuous core. In the laboratory, the samples were repacked to bulk densities measured from undisturbed samples within the same geologic unit exposed in nearby trenches. Each sample remained in the same sample ring for both the moisture retention measurements and the saturated hydraulic conductivity measurements. As such, the internal structure of the repacked samples was preserved throughout the sequence of measurements described next.

The main wetting curve (MWC) and the main drainage curve (MDC) for each sample were measured with hanging-column apparatuses and were obtained by running each sample through a complete wetting and drainage cycle. Electrical resistivity measurements were taken, along with gravimetric water content, at each equilibrium point throughout the cycle. Primary drainage curves (PDCs) were also measured on the samples following the MWC and MDC measurements. In contrast to the MDCs, the PDCs were initiated after the samples were flushed with carbon dioxide (CO_2) and imbibed with deaerated water under a vacuum to assure complete saturation. Data from all three types of pressure saturation curves were used to obtain the unsaturated parameters for Equation 2-1 using RETC, a specialized curve fitting program written specifically for this purpose (van Genuchten 1991).

After completing all moisture retention measurements, the samples were saturated under a vacuum after flushing with CO_2 to ensure complete saturation in preparation for K_s measurements. For sandy and gravelly samples, saturated hydraulic conductivity was measured using constant-head permeameters whereas falling-head permeameters were used for samples rich in clay with low permeabilities. See Brainard et al., (2005) and Baker (2001) for more detailed tables giving the measurements results.

2.4 Infiltration System

The infiltrometer system was designed to deliver a constant flux of water to the soil surface at a flow rate of 2.6 L min^{-1}, or a flux of 2.7 cm day^{-1} across a 3 m by 3 m infiltrometer and to provide a mix of potable water over two-thirds of the infiltrometer and tracer water over the remainder one-third of the infiltrometer during the dye tracer experiments. To maintain steady state conditions, all transitions between potable water and tracer water were accomplished without interrupting flow to the infiltrometer. Insulation within the infiltrometer and a PVC cover minimized water loss and gain from evaporation and precipitation respectively. Flow rates were monitored with a series of data loggers. Brainard et al. (2005) and Hall (2003) give a complete description of the infiltration system.

2.5 Timeline of Infiltration Events

Infiltration began with an extended period of potable water infiltration (Phase 1) followed by two salt tracer infiltration events (phase 2 and 3). NACL was used in both tracer experiments and mixed to a concentration that produced an electrical conductivity of 275 mS/m for the first tracer infiltration event and 1,300 mS/m for the second event. The tracers were infiltrated into a steady state flow field resulting from the extended period of potable water infiltration. A timeline showing the conductivity of the infiltrated water, giving the history of the potable water and tracer events, is given in Figure 2-4.

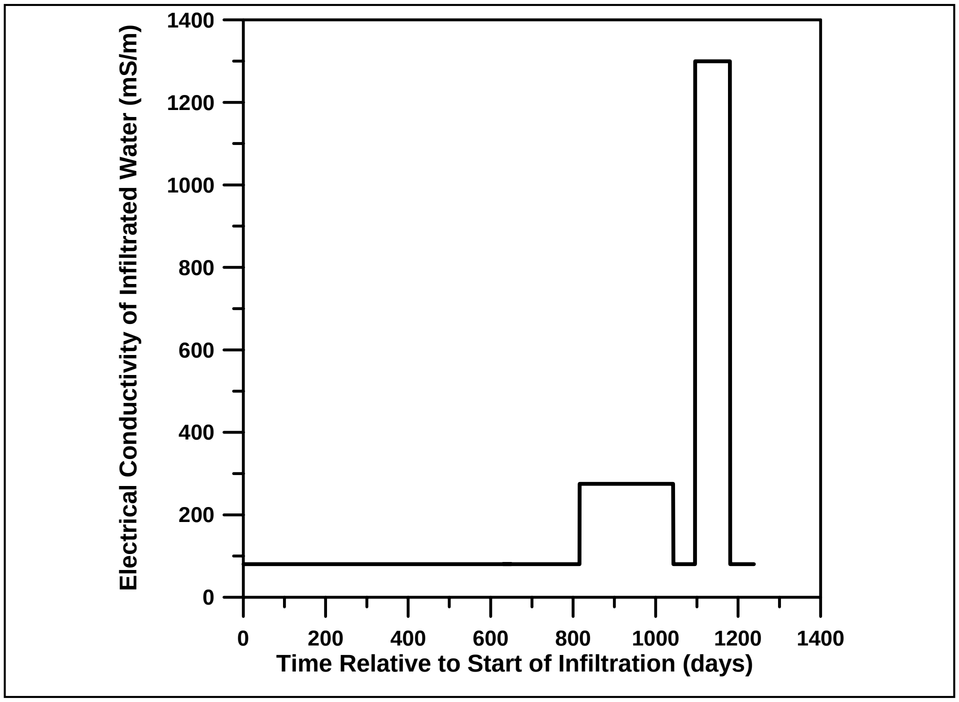

Figure 2-4. Timeline of infiltration events at the STVZ showing the extended period of potable water infiltration between Day 0 and Day 800 followed by the first and second salt pulses, each followed by a short period of potable water flush.

This page intentionally left blank.

3. HYDROLOGICAL MODELING BACKGROUND

3.1 POR-SALSA

Simulations of unsaturated flow and transport of the STVZ infiltration and tracer injections were performed using POR-SALSA, a SNL developed 3-D Galerkin finite element code for simulation of subsurface nonisothermal two-phase flow and transport through heterogeneous porous materials on high-performance parallel computing platforms (Martinez et al., 1997; 2001).

3.2 Flow and Transport Simulations

The ultimate goal in performing both the flow and transport simulations was to obtain results using simulated geostatistical property fields approximating the layered system at the STVZ, with each layer having its unique hydrologic and geostatistical properties. In order to reach that goal, flow simulations were initially based on one and six layer property fields using the hydraulic properties measured and reported by Baker (2000). In order to reduce computational time and to provide multiple scale data sets, these simulations were initially performed using 25 cm grid spacing. Spacing was reduced to 12.5 and eventually 6.25 cm once it became apparent that the simulations produced reasonable results using the coarser grid spacing.

All simulations were based on a 12m by 12m by 12m node centered domain with 0.1, 0.9, and 7.2 million nodes for the 25 cm, 12.5 cm, and 6.25 cm grid spacing respectively. All simulations were run on a supercomputer consisting of 472 Pentium-4 Xeon CPUs, each rated at 3.06 GHz with a 2 Gb/s communication rate through Myrinet packet-communication and switching technology. A total of 70 simulations were run on this supercomputer using these high resolution grids. Run times varied according to grid spacing and the number of processors used. For one-year real time simulations, the run times and number of processors used for each of the three grids are as follows: 25 cm simulations ran to completion within 30 minutes on 8 processors, 12.5 cm simulations in 5 hours on 16 processors, and 6.25 cm simulations in 48 hours on 64 processors.

Flow simulations were performed with the same six-layer property model at the three grids. In this property model, the layers were defined by homogeneous distributions of hydraulic properties within each layer. In an attempt to obtain simulation results that more accurately mimicked the measured moisture content profiles and lateral and downward movement rates of the STVZ than the 6 layer simulations, an ad hoc 29 layer property model was developed by combining measured moisture contents and capillary pressure from the STVZ with laboratory measured properties to obtain properties that might more closely reflect the properties at the STVZ and to provide interpolated values in layers where data was absent. Details of the process used to obtain these properties will be included in a peer-reviewed publication still in formulation. The results are presented here to show the remarkable similarity seen in the trend of the simulated and measured moisture content profiles.

Numerous flow and simulations were completed using both the homogenous layered and geostatistically correlated property models. Most of the flow simulations were performed as part of a sensitivity study which was implemented in an attempt to 1) obtain pre-infiltration initial conditions to post infiltration moisture content changes that more closely approximated the measured data from the STVZ and 2) to better reproduce the rate at which the wetted bulb expanded downward and laterally.

Because the geophysical analysis was based on the results of the fluid flow and transport simulations using geostatistical correlated property fields, the emphasis of this report is on the development of the geostatistical property fields and the results of the flow and transport simulations using these property fields. The next section discusses the development of both the homogenous and heterogeneous property fields with obvious emphasis on the geostatistically-correlated fields.

4. DEVELOPMENT OF HYDROLOGICAL PROPERTY FIELDS

4.1 Layered Homogenous Property Fields

Two sets of homogeneous property fields were developed as a precursor to developing the more complex geostatistically-based property fields. One set consisted of a six layer model in which the stratigraphy at the site was crudely reproduced in layers of constant thickness, with each layer representing one of the six mappable units at the STVZ (see Brainard et al. 2005). The thickness of each layer observed at the STVZ was roughly preserved in the model and the hydraulic properties for each layer was taken as the average values of hydraulic properties measured by Baker (2001) on samples collected within each layer.

The other set of homogeneous property fields consisted of a twenty-nine layer model with each layer being 25 cm thick. The hydraulic properties used in the 29 layer model were derived from a combination of in-situ measured moisture contents and capillary pressures at the STVZ, and hydraulic properties measured from samples collected at the site. These disparate data sets were used to develop pressure saturation curves using Equation 2-1. Assumed correlations between the parameters in Equation 2-1 with measured pre- and post-infiltration steady state pressure field data and moisture profiles from the central neutron access tube at the STVZ were used to obtain parameter values for each of the 29 layers.

4.2 Geostatistically-Correlated Property Fields

4.2.1 Background

Geostatistical simulation techniques were employed to develop random normal distributed, spatially correlated, and synchronized three-dimensional property grids of porosity, Ksat and alpha for use in unsaturated flow and transport simulations with POR-SALSA. Probability density functions were based on the mean and variance of measurements made on samples from the STVZ. Inter-variable correlations loosely based on correlations between the sample measurements were used to spatially synchronize the variables.

The application of geostatistical techniques to hydrologic problems provides the means to expand limited information on the spatial distribution of hydraulic properties in a stochastic manner that is compatible with data ensemble in the spatial context of those data. The basis for geostatistical simulation is the simple and intuitive idea that uncertainty in values become progressively greater at locations further from a know value and that beyond a certain distance the values are uncorrelated. This gives rise to spatial variability structure of the properties with directionally-dependent correlation lengths.

The geostatistical approach involves treating the value of interest as a random variable that falls within probability density functions (pdf), the variances of which increase with the uncertainty, or the distance from a known point. In conditional simulation, the solution is numerically anchored to known or measured property values on the grid and interpolated to other points on the grid. Both the known and measured properties fall within pdfs for that particular variable with each pdf having a distance -from the measuring point-dependent variance. Due to sparsely measured data at the STVZ, the simulations performed for this project were not conditioned on measured data and therefore the simulations were not anchored on known measured values.

In the case of unsaturated flow simulations where several coincident parameters are required for the calculation of unsaturated hydraulic conductivity at each point on a grid, physically consistent relationships among the parameters must be considered in order to obtain physically meaningful synchronization of the coincident parameters. Modeling the spatial distribution of coincident properties without consideration for the inter-variable correlations -that is sampling from separate probability functions for each of the parameters-can lead to highly unrealistic combinations of properties. For example, without such constraints, large hydraulic conductivity values, indicative of coarse grained sediments, may coincide with large absolute values of air entry pressures, when in fact fine-grained sediments produce larger air entry pressures than coarse-grained sediment.

Cokriging and co-simulation methods can be used to simulate property fields where the various parameters are both spatially correlated and inter-variable correlations must be preserved. These methods, however, require sufficient data from which to infer the necessary autocorrelation structures – the spatial correlation between values of the same variable-and cross correlation structures and the spatial correlation between values of different variables. Such data does not exist for the STVZ.

An alternative approach to assure spatial synchronization among parameters is to use assumed statistical correlations between the parameters to constrain the possible range of the parameters at a specific node in the grid. This process involves identifying a primary property to which the other parameters can be correlated. Among the various parameters required for simulating unsaturated flow in porous media, the porosity, saturated hydraulic conductivity (K_s)[L/t], and the van Genuchten alpha (α)[L^{-1}] (Genuchten, 1980) are of particular interest due to their impact on both the initial conditions and the flow field. Of these three properties, the porosity is the most fundamental rock property (primary property) making it the obvious choice to which the other two variables (secondary properties) may be correlated.

Admittedly, correlation between the saturated hydraulic conductivity and porosity in formations and soils may appear absent or may be difficult to discern. However, Baker (2001) showed that a weak positive correlation may exist between porosity and saturated hydraulic in the STVZ sediments. Given that the samples Baker used for these measurements were repacked and that Baker's porosity measurements are likely to have been impacted during the repacking process, this correlation is in question. Since no other data exists allowing for further analysis, we assumed a positive correlation between porosity and saturated hydraulic conductivity.

4.2.2 Geostatistical Simulation Techniques

Simulation of the stochastic hydraulic property models for this project involved a two step process. First, a sequential Gaussian simulation program, SGSIM (Deutsch and Journel, 1998), was used to simulate spatially correlated three-dimensional property fields of porosity, Ksat and, alpha, each field with its own mean and variance, and therefore its own unique cumulative distribution function. Then a *linear model of coregionalization* (Journel and Huijbregts, 1978) was used to spatially correlate the Ksat and alpha fields to the porosity field. The coregionalization method preserves the original spatial correlation structure in Ksat and Alpha as produced the by SGSIM program. SGSIM does have the capability to simulate conditioned fields based on measured properties; however conditioning was not implemented due to very sparse measured data at the STVZ.

The following summary of the *sequential Gaussian simulation* algorithm, as implemented in the GSLIB software routine SGSIM (Deutsch and Journel, 1998), is modified from Routman and McKenna (1997) to reflect the slightly different application to this project.

1. The user supplies a mean and variance and the correlation structure of the variable being simulated. Here the means and variances were calculated from measured values from samples collected at the STVZ while the horizontal and vertical correlation lengths were assumed to be 240 and 24 cm respectively during the initial simulations and were systematically altered in later simulations during a sensitivity study.
2. All data values are converted to a univariate standard-normal distribution (with a mean of zero and a variance of 1) using a graphical normal-score transform as implemented in NSCORE (Deutsch and Journal, 1998). This transformation simplifies the process of generating simulated values while preserving the original spatial correlation structure.
3. The variogram of the normal-score-transformed data is calculated and a variogram model defining the spatial continuity structure is fitted to this variogram. For the unconditioned case, the variogram model is calculated using the user-supplied mean and variance of the variable. The spherical variogram model was used to simulate all property fields.
4. The normal-score transformed data are mapped onto a regularly spaced modeling grid and the conditioned nodes, if present, are flagged so that the data values remain unchanged throughout the simulation process.
5. The user provides a seed number that determines a random path through all un-sampled grid nodes for the sequential simulation process that follows. This seed number is also used to generate the random numbers in step 8 below.
6. At the first grid node along the path, a search is conducted for any “nearby” conditioning data, and after the initial point, the search includes any previously simulated values. The specific definition of nearby points is set by the user, but generally the procedure is to take the nearest 10–12 data or grid-node values up to approximately the range of spatial correlation.
7. The set of nearby points and previously simulated values is weighted by their geostatistical proximity to the node being simulated according to the model of spatial continuity structure (the variogram model) developed in step 2, above. This is simple kriging as described by Isaaks and Srivastava (1989).
8. Under the assumption of a multivariate Gaussian spatial distribution, the weighted average value computed in step 6 and the kriging variance define the mean and variance of the Gaussian conditional probability distribution of the porosity at this location.
9. A value is selected at random from this probability distribution so defined, and assigned as the (normal-score-transformed) value at this point. This value is determined by the seed value mentioned in step 4 above
10. The simulation process moves to the next grid node along the random path defined in step 4 and the generation process begins again as described in step 5. The simulation process is complete when all grid nodes within the model domain have been processed.

11. Following completion of the simulation, the normal score simulated values are back-transformed to “real” porosity space using the histogram of the frequency distribution.
12. Additional simulations are generated by restarting the process at step 4 using a different random number seed value.

In geostatistical terms, the objective of the coregionalization process is to obtain a joint model of two variables such that the spatial relationship described by direct and cross-variable semivariograms for the two variables are satisfied simultaneously, thus assuring spatial synchronization of the secondary variable with the primary variable. Rautman and McKenna (1997) provide a detailed mathematical description as do the original authors Journel and Huijbregets (1978) and Luster (1985). Additional descriptions can be found in Altman and others (1996) and Desbarats (1995; 1997).

This page intentionally left blank.

5. FLOW AND TRANSPORT SIMULATIONS

5.1 Background

Flow simulations for both the layered and geostatistically-correlated property fields were based on the same modeling domain approximating the conditions at the STVZ as much as possible. A combination no-flow and specified flux (Neumann) boundary condition was implemented for the top boundary such that specified flux occurred across a 3 m^2 area –centered within the instrumented area-while evaporation and infiltration from precipitation was prevented across the rest of the domain. The modeling domain formed a cube measuring 12m on each side with no flow boundary conditions specified on the sides and a constant saturation boundary condition specified across the bottom of the domain. The meshes for the homogenous simulations were discretized using finite elements through a simple mesh generation algorithm written by the authors. This algorithm produced orthogonal Cartesian meshes with hexahedral elements. The meshes for the heterogeneous case were produced by SGSIM and spatially coincident variables were synchronized using a linear coregionalization process (see Section 4.2 for details).

5.2 Flow Simulations using Layered Homogeneous Property Fields

5.2.1 Six Layer Simulations

Two sets of properties were used in the layered homogeneous simulations; one for a 6-layer model and the other for a 29-layer model. For the 6-layer model, the hydrological properties were average values measured by Baker (2001) from samples collected within layers (Table 4-1). The results from the 6-layer homogeneous simulations at each of the three grid discretizations, i.e., 25 cm, 12.5 cm, and 6.25 cm, are presented in Figure 5-1. Differences in the simulated results using the three grid resolutions are apparent. The most obvious discrepancies are the slower wetting front velocities, greater wetting front detail, and increased maximum moisture contents near the 7m depth with increased grid resolutions.

Table 5-1: Hydraulic properties used for the six layer homogeneous flow simulations.

Depth (m)	porosity	ln Ksat (m/s)	α (m^{-1})	n	S_r
1.5	0.35	-9.93	0.08	7.69	0.09
0.5	0.34	-11.39	0.13	2.49	0.13
2.0	0.41	-10.27	0.04	5.13	0.18
1.0	0.45	-10.48	0.04	8.67	0.17
1.0	0.38	-11.84	0.09	3.36	0.19
6.0	0.44	-10.08	0.03	6.85	0.12

The measured saturation profiles obtained from neutron attenuation measurements from the center access tube at the STVZ is plotted in Figure 5-2 for comparison (See Brainard et al. 2005 for details concerning the measurements taken at the STVZ). These plots clearly show the faster simulated wetting front advance versus that measured at the STVZ and the greater change in the simulated versus the measured saturation. Note that the high measured moisture content between the surface and 1 meter is attributed to a bentonite-sand plug installed around the access-tube to minimize the likelihood of preferential flow down the access tube well during infiltration (See Brainard 2005).

The lack of detailed agreement between the trends of the simulated and measured field is also apparent. Greater lateral spread as indicated by measured moisture content readings from the STVZ (not presented) is another discrepancy between the simulated and measured data.

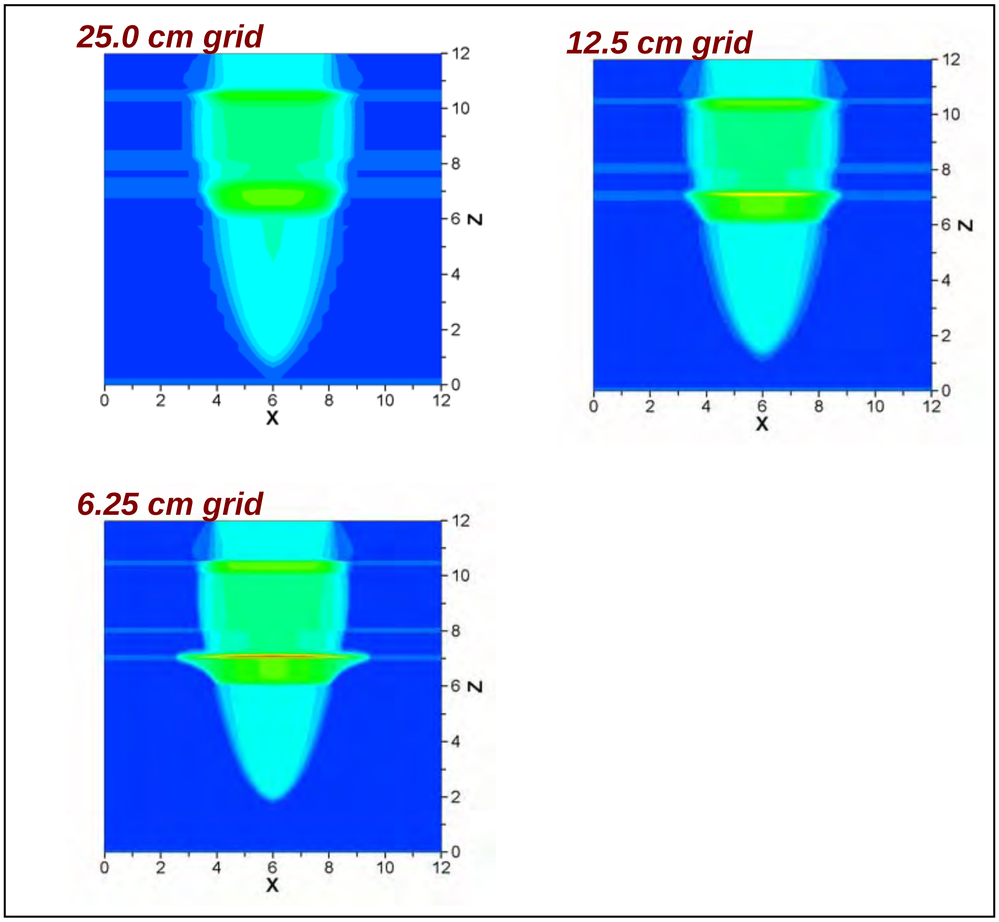

Figure 5-1. **Two dimensional slice showing the moisture content distributions for the 6-layer (homogeneous layers) case at Day 50.**

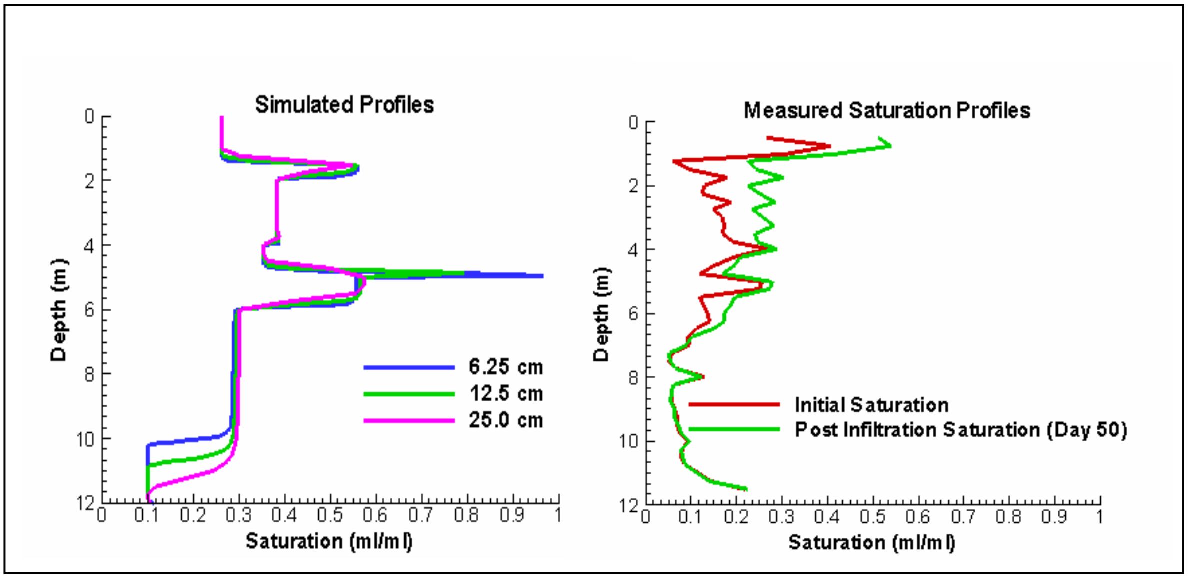

Figure 5-2. **Plots of simulated (left) and measured (right) moisture saturation profiles from the 6-layer homogeneous case. The measured data is derived from neutron moisture meter readings in the center access tube at the STVZ.**

5.2.2 Twenty-nine Layer Simulations

In an attempt to rectify the discrepancies between measured and simulated moisture contents described in the previous section, the 29-layer property field was developed from a combination of in-situ measured field data (capillary pressure and moisture content) and laboratory measured data. The derived parameters are given in Table 5-2. Results from the 29-layer simulation at Day 0 and Day 40 are shown in Figure 5-3 and plots of the simulated and measured moisture content profiles from the center access tube are given in Figure 5-4.

Table 5-2. Hydraulic properties used in the 29 layer flow simulations.

Depth (m)	porosity	Ksat (cm/day)	α (m^{-1})	n	θ_r
1.25	0.31	-4.51	0.00	8.00	0.02
1.50	0.33	-4.63	0.00	8.60	0.03
1.75	0.36	-5.04	0.00	4.60	0.05
2.00	0.35	-4.92	0.00	5.20	0.05
2.25	0.35	-4.91	0.00	6.00	0.05
2.50	0.38	-5.40	0.00	6.00	0.07
2.75	0.36	-5.06	0.00	4.80	0.06
3.00	0.38	-5.23	0.00	5.40	0.06
3.25	0.38	-5.25	0.00	4.50	0.06
3.50	0.38	-5.23	0.00	4.40	0.06
3.75	0.39	-5.46	0.00	3.38	0.07
4.00	0.43	-7.40	0.00	3.60	0.11
4.25	0.40	-5.68	0.00	5.80	0.09
4.50	0.37	-5.19	0.00	2.69	0.06
4.75	0.36	-4.93	0.00	3.50	0.05
5.00	0.43	-9.76	0.00	2.30	0.10

Depth (m)	porosity	Ksat (cm/day)	α (m^{-1})	n	θ_r
5.25	0.41	-5.99	0.00	2.25	0.09
5.50	0.34	-4.80	0.00	4.00	0.04
5.75	0.35	-4.84	0.00	3.69	0.04
6.00	0.35	-4.89	0.00	3.10	0.05
6.25	0.36	-5.06	0.00	3.30	0.06
6.50	0.35	-4.85	0.00	3.00	0.04
6.75	0.34	-4.74	0.00	2.98	0.04
7.00	0.34	-4.75	0.00	3.09	0.04
7.25	0.32	-4.54	0.00	3.30	0.02
7.50	0.31	-4.52	0.00	3.20	0.02
7.75	0.32	-4.59	0.00	3.40	0.03
8.00	0.36	-4.59	0.00	3.20	0.05
8.25	0.32	-4.59	0.00	3.20	0.02

The 29 layer model produced an pre-infiltration moisture content profile that closely matched the measured profile and a post infiltration profile that retains much of the characteristics of the measured data in that the highs and lows in moisture contents of the two curves occur at the same location, yet the simulated moisture contents are significantly higher than the measured moisture contents.

Additionally, the wetting front advance rate is significantly greater than that measured at the STVZ. The lateral spread of the simulated wetting front is more realistic than that of the 6-layer model in that the outer most moisture content profile measurements at the STVZ indicate that the wetting front advanced to this point (7.5 meters from the center of the infiltrometer – data not presented here), but at a much later time than the 40 days shown in Figure 5-4. As mentioned earlier, the high moisture content between the surface and 1 meter is attributed to a bentonite-sand plug installed around the access-tube to minimize the likelihood of preferential flow down the access tube well during infiltration (See Brainard 2005).

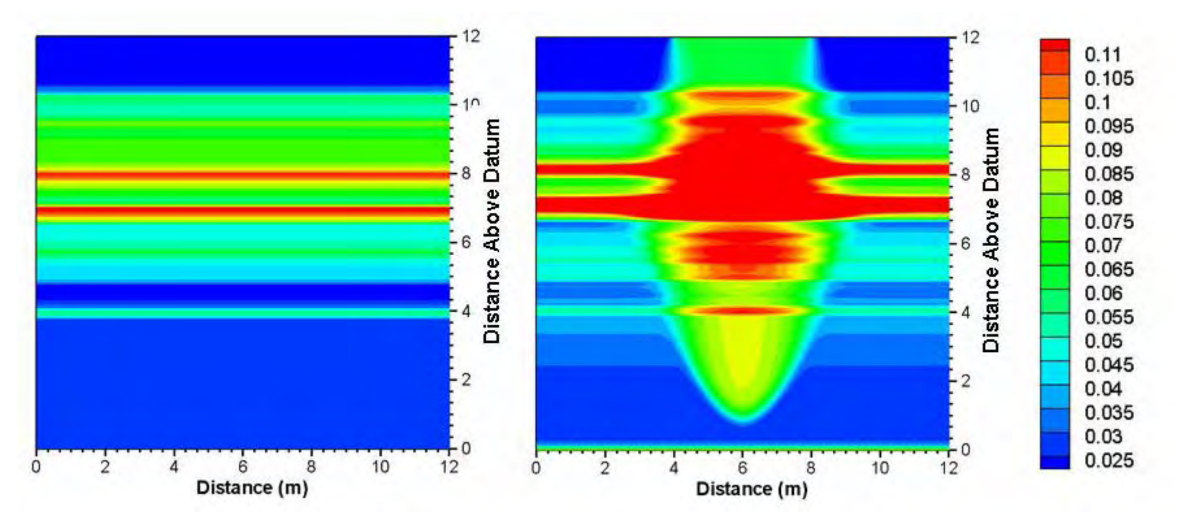

Figure 5-3. **Two-dimensional slice showing the moisture distribution from the 29-layer case (homogeneous layers) simulation at Day 0 and Day 40.**

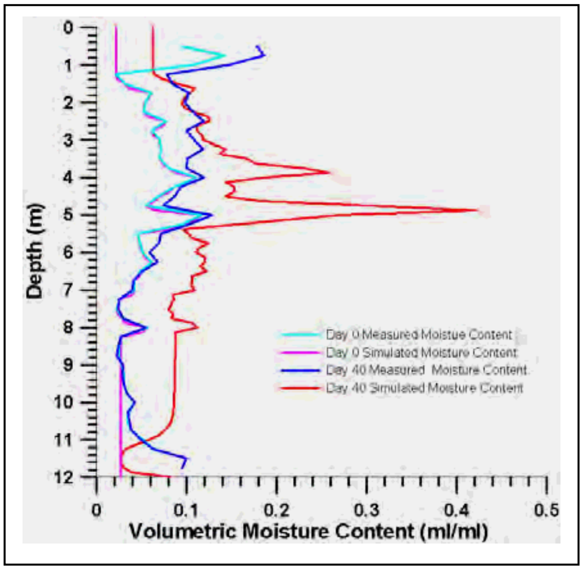

Figure 5-4. **Comparison between the simulated moisture content profiles at Day 0 and Day 80 from the 29 homogeneous case and that measured at the STVZ at Day 40 from the center access tube.**

Simulations based on the 29-layer model were not used in the geophysical analysis portion of this project because they did not incorporate geostatistical property fields. In working with the 29-layer model, additional time was needed to resolve the differences between the simulated and measured field data such that similar wetting front advance rates as well as similar changes in pre and post infiltration moisture contents could be simulated. Accomplishing these objectives would have resulted in a complex 3-dimensional distribution of moisture contents that would have been very representative of the STVZ and would therefore provide a fairly complex test for the geophysical inversion routines. It was our hope to return to the 29-layer model after working with a simpler model which incorporated geostatistically correlated properties and where the discrepancies between the simulated and field measured moisture contents and wetting front advance rates would be resolved before using the more complicated 29-layer model.

5.3 Flow Simulations using Geostatistically Correlated Property Fields

5.3.1 Six-layer Simulations

Geostatistically-correlated property fields used for the geophysical investigations consisted of one-layer and six-layer models. For ease of communication, we refer to these models as the heterogeneous models. The six-layer heterogeneous case used the same properties as the six-layer homogenous case described above and presented in Table 5-1. As described in 4.1 these values are the means of hydraulic property measurements from samples collected within each layer. The standard deviation of these data within each layer which was also calculated from these measured properties. As described in Section 4.2, the saturated hydraulic conductivity (Ks) and the V.G. alpha parameter (α) were coregionalized with the porosity. The mean, standard deviation and assumed correlation between porosity Ks and α are also listed in Table 5-3. Correlation lengths of 20 cm horizontal and 240 cm vertical were used in these simulations. A two-dimensional slice from the simulated three dimensional moisture content distribution for the six-layer heterogeneous case at Day 80 after the start of infiltration is shown in Figure 5-5.

Table 5-3. Hydraulic properties, standard deviations, and correlations used for developing the six-layer geostatistically correlated property fields.

Thickness of Layer (m)	Porosity (std. dev.)	ln Ksat (cm/s) (std. dev.) [correlation*]	α (m^{-1}) (std. dev.) [correlation*]	n	Sr
1.5	0.35 0.07	-9.93 (0.36) [0.68]	0.08 (0.03) [-0.68]	7.69	0.09
0.5	0.34 0.07	-11.39 (0.41) [0.67]	0.13 (0.05) [-0.68]	2.49	0.13
2	0.41 0.07	-10.27 (0.32) [0.68]	0.04 (0.01) [-0.68]	5.13	0.18
1	0.45 0.07	-10.48 (0.32) [0.68]	0.04) (0.01) [-0.68]	8.67	0.17
1	0.38 0.07	-11.84 (0.33) [0.66]	0.088 (0.03) [-0.68]	3.36	0.19
6	0.44 0.07	-10.08 (0.33) [0.68]	0.04 (0.01) [-0.68]	6.85	0.12

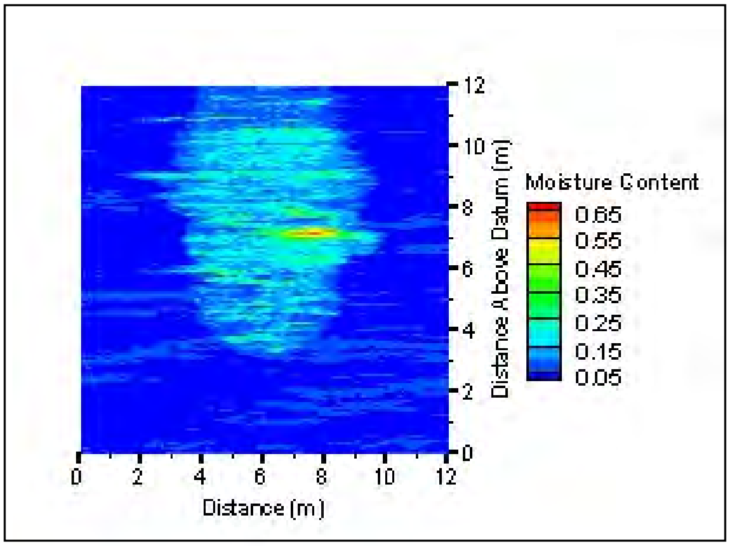

Figure 5-5. **Two dimensional slice showing the Day 80 moisture distribution derived from a 6.25 cm grid discretization and using the six-layer heterogeneous case properties given in Table 5-1.**

In comparison with the six-layer homogenous case shown in Figure 5-1, the heterogeneous property field appear to decrease the vertical wetting front advance rate while increasing the rate of lateral spread. As was the situation with the 6-layer homogenous case, the simulated six-layer heterogeneous simulations result in a larger change in moisture content between pre- and post-infiltration conditions than that measured from the center access tube (see Figure 5-6). As mentioned earlier, the high moisture content between the surface and 1 meter is attributed to a bentonite-sand plug installed around the access-tube to minimize the likelihood of preferential flow down the access tube well during infiltration (See Brainard 2005).

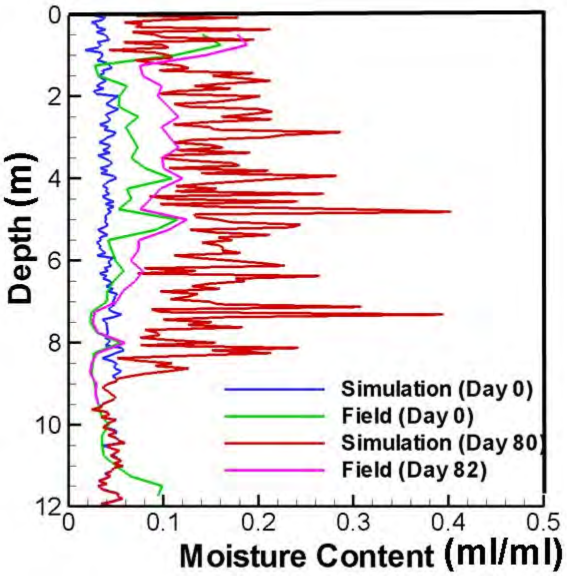

Figure 5-6. Comparison between the simulated moisture content profiles at day zero and 80 from the 6 layer heterogeneous case and that measured at the STVZ at comparable days from the center access tube.

5.3.2 One-Layer Simulations

In an effort to reduce the discrepancies between the measured change in moisture contents at the STVZ and the simulated changes, numerous subsequent simulations were performed using 25 cm grid spacing and a one-layer heterogeneous property field to empirically determine which properties and parameters required adjustment to reduce the discrepancy between simulated and measured moisture contents. This parameter study involved running a simulation on a base case of hydraulic properties and geostatistical parameters to obtain results that subsequent simulations could be compared to. Subsequent simulations incorporated property fields that resulted from altering the value of one of the many parameters in the VG equation, $\theta_r, \theta_s, \alpha, n$ as well as K_s or the variance of the property. In this study, the residual moisture content (θ_r) was also treated as spatially random property and were coregionalized with porosity as was the case with the other parameters. Correlation lengths were also altered from 20 cm vertical and 240 cm horizontal to 75 and 750 respectively. As with all the simulations, isotropic distributions of properties were assumed in horizontal planes.

These last two properties were also varied during the parameter study. All the flow simulations for this parameter study were run on a 25 cm spacing. Each of the simulated flow fields were qualitatively evaluated for the impact that altering each parameter or hydraulic property had on the simulated flow field. Through a process of elimination, simulations using the parameters listed in Table 5-2 were chosen as the starting point for the geophysical analysis. A simulation result at Day 40 is plotted in Figure 5-7 and a comparison between the simulated and field measured moisture contents are given in Figure 5-8.

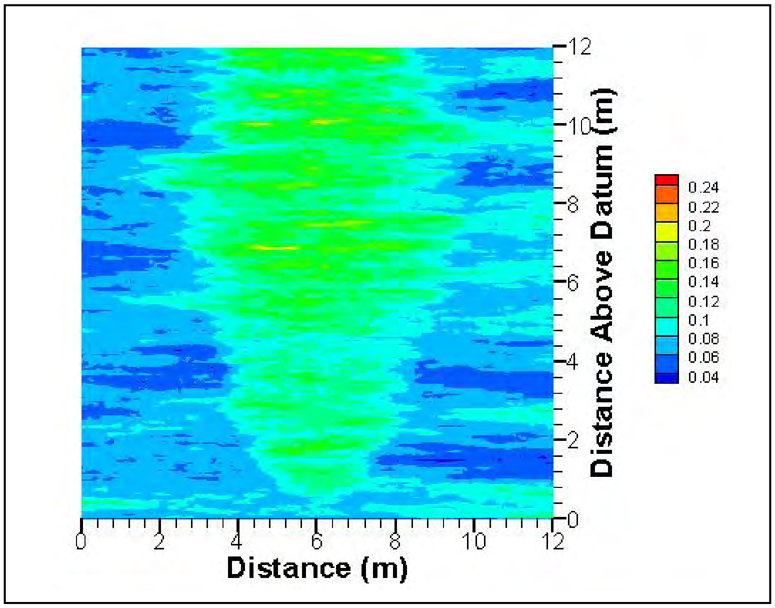

Figure 5-7: Two dimensional slice showing the Day 40 moisture distribution derived from a 6.25 cm grid discretization and using the “Final Case” properties given in Table 5-2.

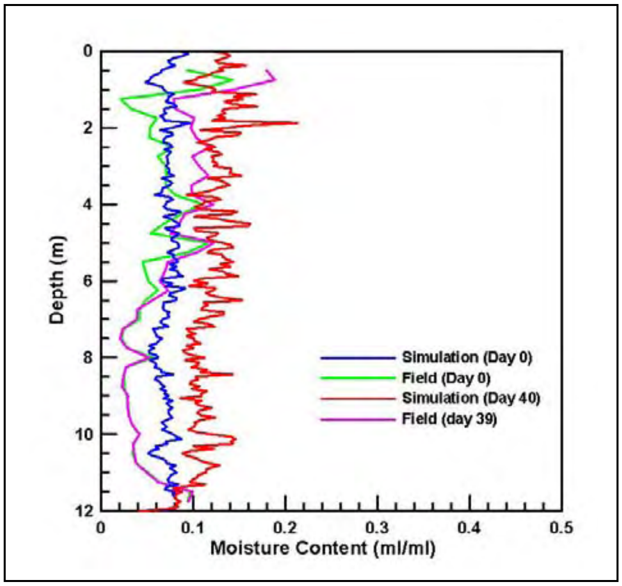

Figure 5-8: Comparison between the simulated moisture content profiles at day zero and 40 from the parameter study “Final Case” and that measured at the STVZ at comparable days from the center access tube.

Table 5-2. The base case and final case of parameters used for the geophysical analysis.

	Porosity (Std. Dev)	ln Ksat (m/s) (Std. Dev.) [Correlation]	ln Alpha (cm^{-1}) (Std. Dev.) [Correlation]	n	Sr (Std Dev) [Correlation]	Corr. Lengths (cm) (horiz.) [Vert]
Base Case	0.42 (0.48)	-5.98 (0.83) [7.0]	-3.11 (0.57) [-7.0]	3.35	0.154 (0.02) [0.7]	(750) [75]
Final Case	0.42 (0.48)	-3.36 (0.83) [0.7]	-3.11 (0.29) [-0.7]	3.35	0.154 (0.02) [0.7]	(750) [75]

A comparison of the simulated and field measured moisture content profiles shows that the initial and final simulation measurements roughly fall within the range of the measured data between 1 and 6 meters and overestimates the initial moisture contents below 6 meters. In contrast to the 6 layer heterogeneous case where the simulated moisture content profile seemed to roughly follow the trend of the measured profile, here there is no such resemblance. The different wetting front locations are another discrepancy between the simulated and measured data. The measured data indicates that the wetting front was near 7 meters at day 40, while in the simulation the wetting front was at 11.5 meters.

As mentioned earlier, the high moisture content between the surface and 1 meter is attributed to a bentonite-sand plug installed around the access-tube to minimize the likelihood of preferential flow down the access tube well during infiltration (See Brainard 2005).

5.4 Transport Simulations

A series of transport simulations designed to duplicate the tracer experiments at the STVZ provided additional data sets for geophysical analysis. The transport simulations were initiated on the “Final Case” simulated steady state flow filed discussed in the previous section. The dispersion and diffusion properties used in the transport simulations are listed in Table 5-3. The infiltrated concentration of the tracer (C/Co) was taken as 1 and the solution was infiltrated across all arrays within the 3 by 3 m infiltrometer (See Section 2). Simulation results are presented in Figure 5-9 showing the C/Co concentrations through a two dimensional slice at Day 40 of the tracer test. The concentrations are greatest near the infiltrometer and taper off more rapidly in the horizontal than the vertical direction, i.e. the tracer plume elongated in the vertical direction.

Table 5-3: Material Properties used in the transport simulations.

Longitudinal Dispersivity (m)	Transverse Dispersivity (m)	Diffusion Coefficient (m^2s^{-1})
0.5	0.5	$1X10^{-12}$

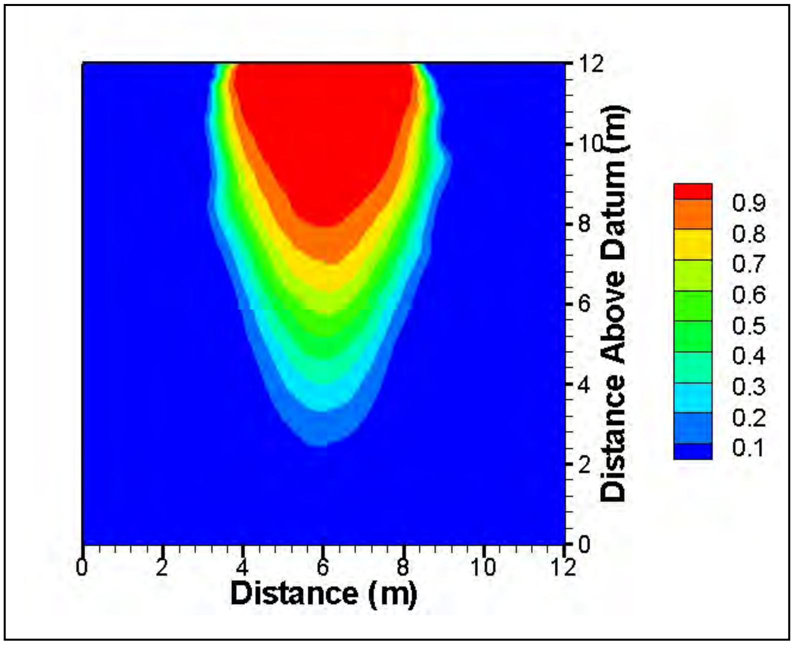

Figure 5-9: Two dimensional slice showing the Day 40 tracer concentration (C/Co) distribution derived from a 6.25 cm grid discretization and using the material properties in Table 5-3.

This page intentionally left blank.

6. ANALYSIS OF ERT INVERSION

6.1 Introduction

The hydrological models developed and simulated at SNL and used in the ERT study were based on much higher grid resolutions than are possible with ERTimaging. Using these high-resolution models allows for investigating how intrinsically low-resolution ERT images relate to true, complex stochastic hydrological scenarios. The hydrological models were intended to represent the character of the STVZ and evolved through an increasingly complex representation of the site. The models mimicked site scenarios and included following the progress of infiltration and solute tracers. As discussed in previous sections, several rounds of models were pursued while trying to resolve discrepancies between field-measured and simulated hydrological results.

One problem was that the hydrological simulations differed from field measurements in having higher saturations, higher saturation contrasts between pre-infiltration and post infiltration moisture contents, and more sharply defined infiltration zones. This was an area of concern because the conversion of the hydrological parameters (moisture content) to geophysical parameters (resistivity or conductivity) amplifies these effects. For this reason, the results presented in this section concentrate on the latest set of infiltration and solute transport models that present the closest approximation to site conditions. As discussed in Section 5.3, these models incorporated a 6.25 cm grid spacing and infiltration was simulated for one year to obtain a steady state flow field. For the solute transport simulations, a solute was introduced into the steady state flow field at the end of one year. Selected time increments, typically 10-day or 30-day intervals were extracted for the purpose of modeling with ERT.

ERT modeling consists of these steps:

- First, the hydrological model was translated to resistivity using an empirical Archie-like equation with parameters derived from the original STVZ experiments.

- Second, the hydrological model was padded appropriately to permit forward modeling. Additional pads were generated by repeating the value of the edge-most cells in X, Y and Z directions a number of times, determined from experiments described below, and using smoothly increasing cell sizes, to provide the ‘whole-earth’ required by the ERT modeling software.

- Third, a forward model consisting of generation of V/I data for every electrical data point in the original dipole-dipole STVZ data collection schedule was generated using 31,444 data points. To simplify translation between meshes of different resolution, a somewhat idealized electrode distribution was used rather than the true distribution present at the field site. However every electrode present at the field site was represented in the synthetic models (282 electrodes in 8 wells with 15 electrodes each and an assortment of surface electrodes).

- Normally distributed 3% random noise was added to the forward modeled data.

- The forward ERT data were then inverted on coarse meshes (37.5 cm foreground area) similar to those used for the original project. Mesh parameters were varied as described below in an attempt to improve the modeled result.

In order to accommodate very large meshes, it was necessary to isolate a forward modeling only version of the finite-difference code. This change permitted modeling of 242 X 242 X 250 (14,641,000 element) meshes in 35 hours on a 3.4 GHz Pentium IV desktop computer with 3 gigabytes of RAM running on Microsoft® Windows XP Professional.

6.2 Improvements to ERT Modeling

6.2.1 Calculation of Resistivity From Hydrological Models

For clean sediments, those with no clay minerals, Archie's relation (Archie, 1942) yields estimates of the bulk resistivity ρ_b from the porosity and fluid conductivity:

$$\rho_b = F\rho_w S^{-m}, \tag{6-1}$$

where, S is the saturation, and m is the saturation exponent, usually assumed to be equal to 2. The fraction of the pore-space filled with fluid F is called the formation factor and is given by:

$$F = a\phi^{-n}, \tag{6-2}$$

where a and n are constants and ϕ is the formation porosity. A local empirical model which yields the bulk electrical conductivity in terms of a, water content θ, and the water electrical conductivity σ_w assumes that the exponents for porosity and saturation are the same, is expressed in terms of electrical conductivity and moisture content ($\theta = \phi * S$) was

$$\sigma_b = a\sigma_w\theta^b, \tag{6-3}$$

where the value of $a\sigma_w$ was 1.1 and b was 1.6; values derived empirically from the STVZ field experiments. For the transport models, an addition factor was applied based on the mass fraction T_{mf} of solute added and a transport factor T_{factor}. This was calculated using the formula:

$$\sigma_{b'} = \sigma_b * \left(1 + T_{mf} * T_{factor}\right), \tag{6-4}$$

and the transport factor was assigned the value 3.

6.2.2 Forward Modeling Considerations

The distribution of the electrical potential in the earth is governed by the continuity equation,

$$\nabla \bullet \hat{\sigma}\, \nabla \mathrm{V} = \mathrm{I}, \tag{6-5}$$

where V is the scalar electrical potential and I is the distribution of electric current sources in the media. The forward electrical resistivity calculations were carried out using an anisotropic version of the finite-difference formulation of Dey and Morrison (1979) to solve for the potentials in Equation (6-5) at a pair of receiver electrodes given within a 3-D anisotropic earth. One difficulty in applying the finite-difference method to modeling resistivity data is that we must approximate a region of essentially infinite extent in the X, Y, and +Z directions using a mesh with limited extents in these directions. The approach used in this routine is to use the "non-reflective" boundary conditions given by Dey and Morrison, 1979. These boundary conditions provide only a rough approximation to a semi-infinite domain. Therefore, it is still necessary to include a number of mesh elements outside the region of interest. We refer to these additional cells as <u>padding cells</u> and the portion of the finite-difference mesh containing the padding cells as the <u>background region</u> as opposed to the <u>foreground region</u>, the area we wish to image.

Generally, the numerical accuracy is improved by making the background region as large as possible. However, extremely large background regions increase the computational effort. Also, in increasing the size of the mesh, it is important that the resulting system of equations not become unstable or in mathematical terms <u>ill-conditioned</u>. Ill-conditioned systems tend to amplify errors thus a badly designed large mesh may have greater errors than a smaller mesh. For example, it is generally unadvisable to change the size of the cells rapidly so that very large cells are immediately adjacent to very small cells. It is also generally best to keep cells more or less equidimensional as very long, thin cells tend to make the system ill-conditioned (see below). Thus the background regions usually starts with a layer of pad cells the same size as the cells of the foreground region and the size of the pad cells is increased progressively outward and away from the foreground. To determine appropriate mesh parameters, we ran a series of experiments comparing forward solutions from a series of finite element meshes with the analytic solution for a 100 ohm-m half space. The results indicate the following:

1. The maximum element aspect ratio should be as small as possible (Figure 6-1a). We determined that 10:1 resulted in over 80% of the forward data being accurate to 1%. These numbers dropped to 70%, 50% and 10% for 16:1, 32:1 and 64: 1 aspect ratios. Interestingly, for all aspect ratios modeling error was <6% for 92% of the data.

6.2.3 At a background region size of 5X, the foreground region size resulted in >80% of the finite difference data being accurate within 1% (Figure 6-1b). These numbers dropped to 65% and 40% for 3X and 2X ratios. However, there was no improvement moving to 7X. Further experiments showed that increasing the Z background dimension at the expense of the XY background dimensions was an effective method to further decrease the overall mesh size. Rations of 3X in XY appear to be acceptable when coupled with a ration of 4X-5X in Z. Inverse Modeling of ERT Data

This project used the same modified Occam's inversion routine used previously to invert data from the STVZ. These results were compared with those for a newer inversion strategy. The objective function, the objective function minimized using both inversion routines, is given by

$$\mathbf{S}(\mathbf{m}) = (\mathbf{d}_{\mathrm{obs}} - \mathrm{g}(\mathbf{m}))^{\mathrm{T}} \mathbf{W}_{\mathrm{D}} (\mathbf{d}_{\mathrm{obs}} - \mathrm{g}(\mathbf{m})) + \alpha\, \mathbf{m}^{\mathrm{T}} \mathbf{R} \mathbf{m}\,, \tag{6-1}$$

where **d** is the vector of data values, **m** is the vector of parameters, **g**(m) is the forward solution, $\mathbf{W}_{\mathrm{D}}$ is the diagonal data weight matrix, **R** is the regularization operator which is discussed in more detail below, and $\mathbf{d}_{\mathrm{obs}}$ is the vector of observed data. α is an empirical factor that controls the amount of regularization versus the fit of the forward model to the data. Minimizing the objective function for a large value of α results in a smooth solution but a poor data fit. The optimal solution corresponds to the largest possible value of α which still fits the data to some a-priori value. LaBrecque et al. (1999) discuss a method of iteratively determining α for 3-D inversion used for the older algorithm. In the new algorithm, a trial-and-error approach is used at each iteration to find an optimal value of α that gives rapid but smooth convergence. The parameters, **m**, are the natural logarithms of the three components of conductivity (X, Y, and Z) of each cell in the finite-difference mesh.

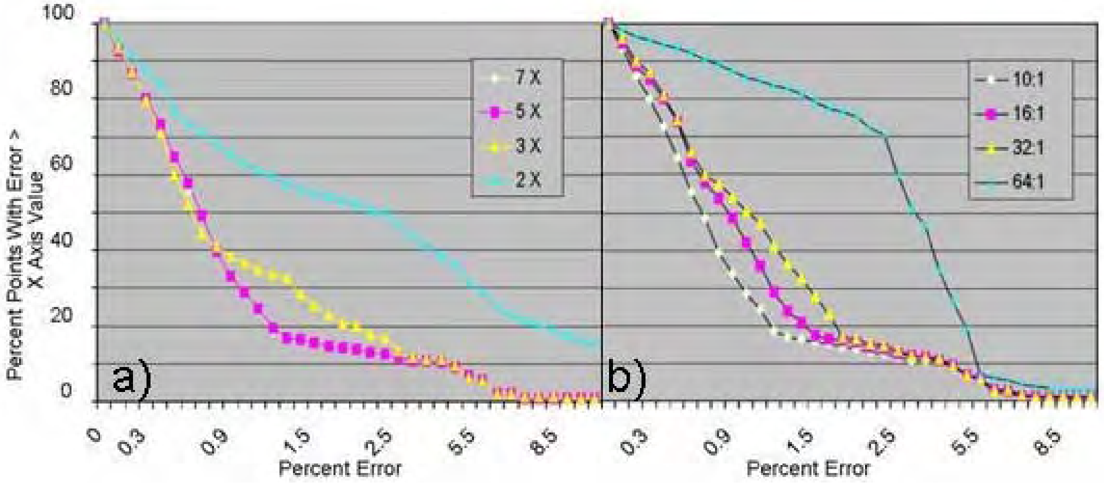

Figure 6-1. Finite-difference forward model error relative to the analytic result for a 100 ohm-m half space for trials of (a) background to foreground ratios and (b) pad element elongation ratio.

The nonlinear iterations can be expressed as $\mathbf{m}_{n+1} = \mathbf{m}_n + \Delta\mathbf{m}_n$. The parameter change vector at n^{th} iteration, $\Delta\mathbf{m}_n$, is obtained by solving the linear system

$$\left(\mathbf{G}_n^T \mathbf{W}_D \mathbf{G}_n + \alpha\mathbf{R}\right)\Delta\mathbf{m}_n = \mathbf{G}_n^T \mathbf{W}_D \left(\mathbf{d}_{obs} - g(\mathbf{m}_n)\right) - \alpha\mathbf{R}\mathbf{m}_n , \tag{6-7}$$

where the elements of the sensitivity matrix, $\mathbf{G}^\mathbf{T}$, are given by

$$\mathbf{G}_\mathbf{n}^\mathbf{ij} = \left.\frac{\partial \mathbf{g}^\mathbf{i}(\mathbf{m})}{\partial \mathbf{m}^\mathbf{j}}\right|_{m_n} . \tag{6-8}$$

The system of equations given by Equation (6-6) is positive-definite and is solved using the conjugate-gradient method with a diagonal preconditioner (LaBrecque et al., 1999). A data-error reweighting scheme is implemented to suppress the effects of data outliers (Morelli and LaBrecque, 1996).

6.3 Modeling of Synthetic Hydrological Data

Synthetic hydrological infiltration models were created at 0, 10, 20, 30, 61, 91, 181, and 361 days of infiltration into an STZV-like model having a mesh size of 6.25 cm. After converting to resistivity and padding the mesh, forward ERT responses were calculated and noise was added. The noisy forward data were inverted on a 37.5 cm mesh. For comparison, we compressed the original high resolution model derived from the conversion of the hydrological data from 6.25 cm cells to 37.5 cm. We applied an anisotropic average formula. For example, the X-component R_X of resistivity for the 37.5 cm cells is given by

$$R_X = 1 \Bigg/ \frac{\sum_{k=1}^{6}\sum_{j=1}^{6} 1 \Big/ \frac{\sum_{i=1}^{6} R_{ijk}}{6}}{36}, \qquad (6\text{-}9)$$

where $R_{i,j,k}$ is the resistivity of the 6.25 cm cells contained in the 37.5 cell *i, j, k* are the indices in the X, Y, and Z directions respectively. Y- and Z- components are calculated similarly. We make both visual and statistical comparisons of the hydrological models and ERT images from inversion of the synthetic data. When performing statistical comparisons using semi-variograms, the purpose of the plot is to indicate directional rates of change. One can summarize semi-variograms in terms of the overall variance: the value that the semi-variogram approaches asymptotically for large offsets, the correlation length, the offset distance at which the curve approaches its final asymptote, and the form of the semi-variogram between the zero offset and the correlation length. Because variance of a block of averaged values is always less than the variance of the individual values, the semi-variograms of the compressed images are always lower than the semi-variograms of the high-resolution images. Ideally however, the form and correlation length will appear the same.

6.4 Comparison of Synthetic Models

The old and improved inversion methods were compared using the synthetic dataset. We compared the old inversion method with the old mesh, the old inversion method with the new mesh, and the new inversion method with the new mesh. Results for the background are compared statistically in Figure 6-2 using a semi-variogram in the X and Z directions. In each case, the least variance and most accurate sill is identified in the X direction. The sill of the compressed model drops relative to the sill of the uncompressed model, confirming this is the expected behavior as the resolution of the model decreases. The sill of the original mesh inversion is the lowest of all presented, indicating that the improvements to the inversion described have increased the resolution in the model.

This improvement in resolution can be seen in the images. The results at Day 20 and Day 361 are presented in Figures 6-3 and 6-4. The old padding scheme underestimated the intensity of wetting and did not accurately resolve the water location, particularly at depth. The newer inversions show similar results and demonstrate significant improvement both in terms of absolute intensity and accuracy in location of the wet area.

In Figure 6-5, we compare the resolutions of the 6.25 cm (Figure 6-5a) and 37.5 cm (Figure 6-5b) meshes by showing the raw data for 181 days. Although the ERT forward data were calculated from the 6.25 cm mesh, the 37.5 cm mesh image in Figure 6-5b represents the best that one could hope to extract from the ERT using a 37.5 cm inversion mesh. Figures 6-5c compares the inverted result from the new inversion method beside the 37.5 cm version of the original model (Figure 6d) for 181 days of infiltration. Although the models are smooth with respect to the original, the essential

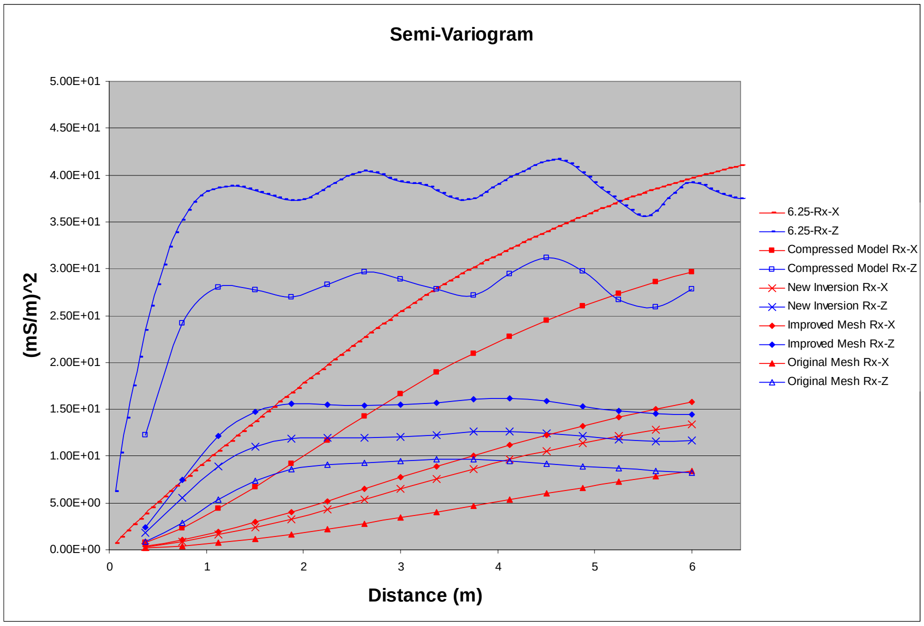

Figure 6-2. Semi-variogram of the background synthetic model showing results over 6 meters for the uncompressed, 6.25 cm model (horizontal line); the hydrological model compressed 37.5 cm grid (squares); and inversion results on the 37.5 cm mesh for the new inversion method (x's); Occam's inversion with improvedpadding (diamonds); and Occams' inversion with the same mesh used for the original STVZ field study (triangles). Semi-variograms for the Z direction are shown in blue and the horizontal direction in red.

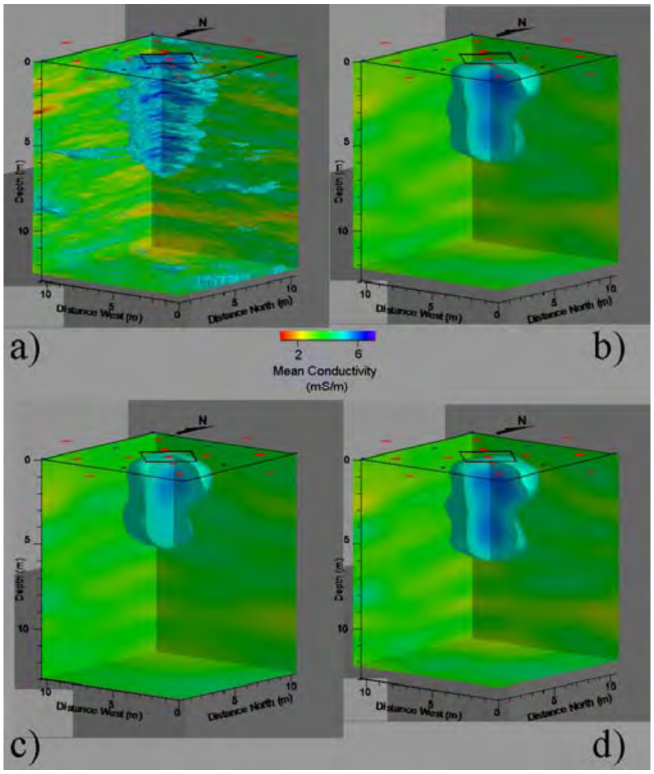

Figure 6-3. Visual comparison of Day 20 synthetic infiltrations showing (a) 6.25 cm hydrological model converted to conductivity, (b) new inversion method, (c) Occam's inversion with the STVZ mesh, (d) Occam's inversion method with improved pad scheme.

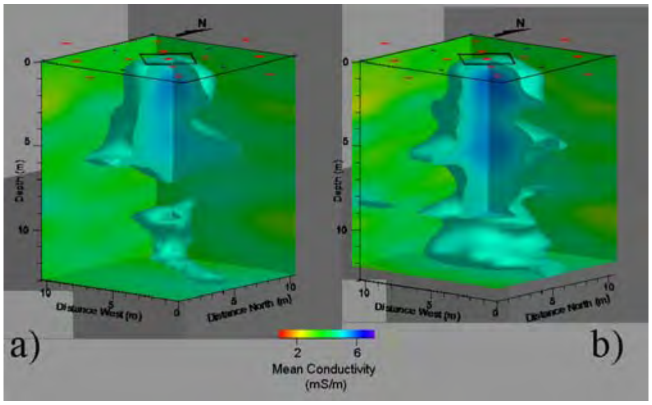

Figure 6-4. Visual comparison of Day 361 synthetic infiltrations showing (a) STV field – style mesh (b) ultimate, new inversion method.

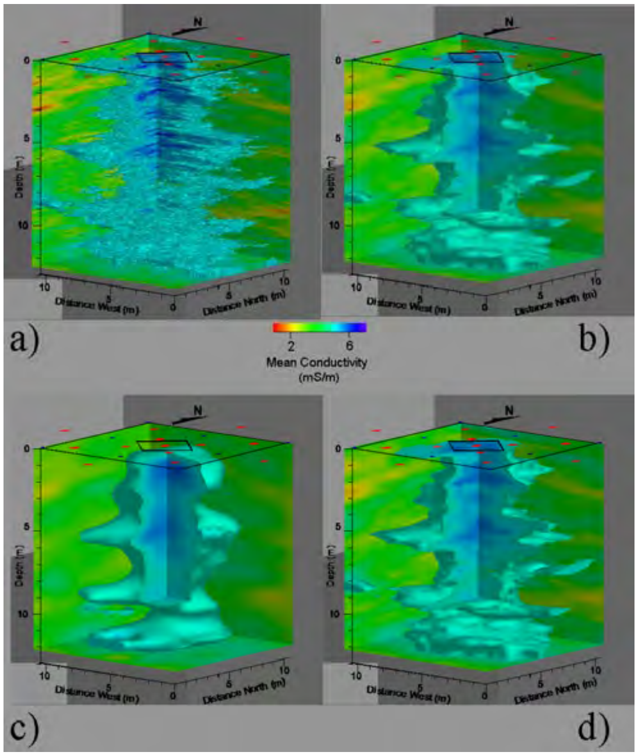

Figure 6-5. **(a) High resolution 6.25 cm model; (b) and (d) 37.5 cm compression of model in (a); the image in (c) shows the result of the new inversion method for 181 days.**

character of the infiltrated water is well-represented. The resolution of the inversion appears to be on the order of .75 m. The inversion does show the water extending all the way to surface nor does it provide fine resolution of horizontal layers. Also, some conductive areas that are likely inversion artifacts of the have been smoothed away.

Similarly, synthetic transport models were based on the Day 361 infiltration model. Hydrological models were generated for 0 (= 361 days of infiltration), 2, 4, 6, 8, 10, 20, 30, 40, 60, 80, 90 and 100 days of infiltration. Figures 6-6a and 6-6b compare the ERT inversion to the raw 37.5 cm compressed data for 20 days Figures 6-6c and 6-6d show the inversion after

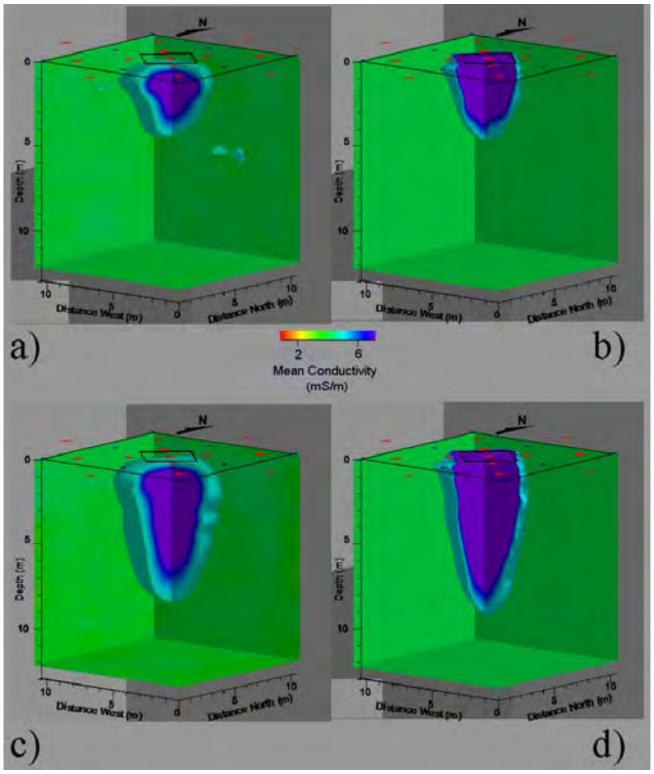

Figure 6-6. Transport models showing (a) inverted result and (b) inverted model at Day 20; and (c) inverted result and (d) synthetic model at Day 50.

6.5 50 days of transport infiltration. While the conductive zone is somewhat broader than the original, the depth of penetration and overall conical shape are well represented. Conductive volumes represented are probably fairly similar since the outer rim of the broad conductive area in the ERT images is represented by lower conductivities. As noted earlier, the hydrological models show higher saturations and larger contrasts in saturation than those observed at the STVZ (see for example Figures 5-2, 5-4) and the infiltration region is more sharply bounded (Figures 5-1, 5-3). When these models are converted to resistivity, the result is that the conductive (infiltration) area of the synthetic model has a larger contrast and is more sharply defined than those observed in the field. From our experience,the smooth-model ERT would provide an even better representation of an actual field infiltration than is demonstrated here since field conditions tend to produce more gradual boundaries than the hydrological models When the difference-inversion technique (LaBrecque and Yang; 2001) was employed (Figure 6-7), it succeeded in modestly improving the

inversion image. However, the magnitude of the conductivity increase in the synthetic model precluded dramatic improvement because this technique is designed to improve subtle changes in models. Portions of the conductive zone now extend to surface and the 'bullet' is tighter and more pointed.

6.5 Comparison of Models and Quantification of Improvements

The final stage of the project was to compare inversion results from the Occam's inversion with images from the new inversion method to quantify any improvements in the imaging technique.

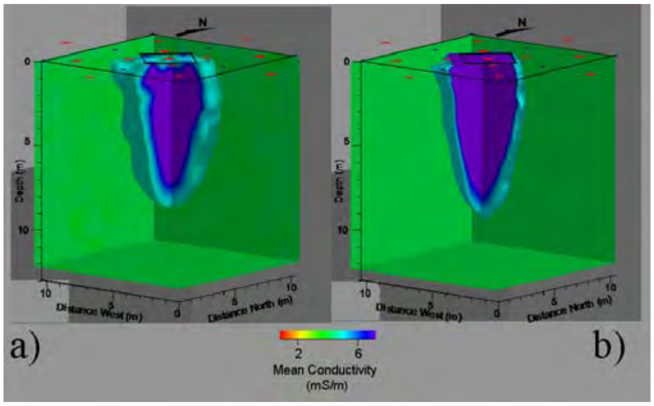

Figure 6-7. Difference inversion of synthetic transport model at Day 50 showing (a) new inversion result and (b) 37.5 cm compressed synthetic model.

One enhancement to field technique not previously discussed in the literature (2) is temperature correction. (Note: All field results discussed are temperature corrected.) Temperature correction was applied using Arps' Equation, expressed below in terms of electrical conductivity and temperature, given in Centigrade:

$$EC_2 = EC_1 \frac{T_2 + 21.5}{T_1 + 21.5} \tag{6-10}$$

During the experiment, the temperatures changed substantially on an annual basis. These changes originate from two sources: a) annual changes of heat conduction from the surface and b) advection of heat in the infiltrating water. Over the course of a year, the average temperature of the water being infiltrated ranged from about 6 C to nearly 27 C; a difference in temperature of more than 20 C.

Figure 6-8 shows the importance of temperature correction by comparing images of temperatures with corrected and uncorrected electrical conductivity for two dates during the first saline injection test. The dates of October 1, 2001 and January 31, 2002 were chosen to be late enough in the injection test so that the hydrological conditions, such as moisture content and salinity, were expected to be similar, but the temperature patterns at the site very different. The peak, annual surface temperatures in Socorro occur in mid July. Because of the lag time for conduction and convection of heat into the subsurface, October 1, 2001, was chosen as the peak temperature at a depth of a few meters. Lowest temperatures on the site occur in mid-January. To provide a basis for comparison, January 31, 2002 was chosen since it represents the last coldest data collected prior to discontinuing the first tracer injection.

Comparing the uncorrected conductivity images, (Figures 6-8a, 6-8c) the conductive region is significantly larger in lateral extent and intensity on October 1 than on January 31. Without temperature corrections, these results would imply, erroneously, that the extent and concentration of the tracer has somehow decreased in spite of the continued, consistent injection over the intervening months. Removing the effects of temperature (Figures 6-8b, 6-8d), shows that the tracer concentration has increased below the infiltrometer. However the area affected is somewhat illogically spread at surface and does not penetrate to depth.

The new inversion method provided significant further improvement. The images shown Figure 6-6 may be compared, in temperature corrected form, with images generated from the new inversion method for the same dates (Figures 6-9a and 6-9b). At this point, the tracer has not only increased in size under the infiltrometer, but its position is more consistent and the overall depth affected is increased.

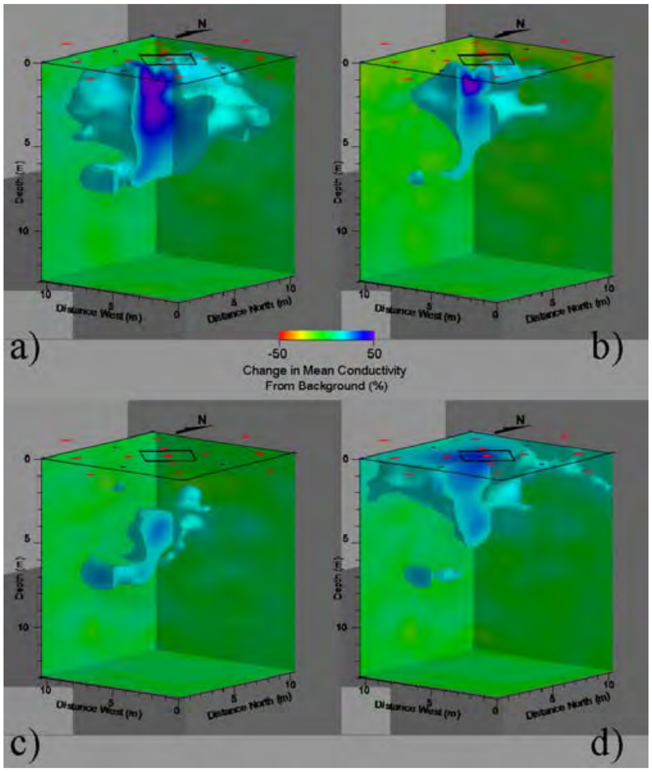

Figure 6-8. **Occam's inversion of STVZ transport data showing (a) uncorrected image of 10/01/01 data (b) image of temperature corrected 10/01/01 data, (c) uncorrected Occam's inversion image of 01/31/02 data, and (d) temperature corrected 01/31/02 image.**

6.6 Conclusions

High-resolution (6.25 cm) Synthetic hydrological models were converted to synthetic resistivity models to establish the resolving capability of ERT collected using a much coarser electrode spacing (75 cm). Improvements in ERT inversion strategy included enhanced padding of meshes, and application of improved forward modeling and inversion strategies that have evolved since the field studies. Improvements in data treatment include the application of temperature corrections to the inverted data. Improvements in the forward modeling mesh had a significant impact on the quality of the images within the inversion routine.

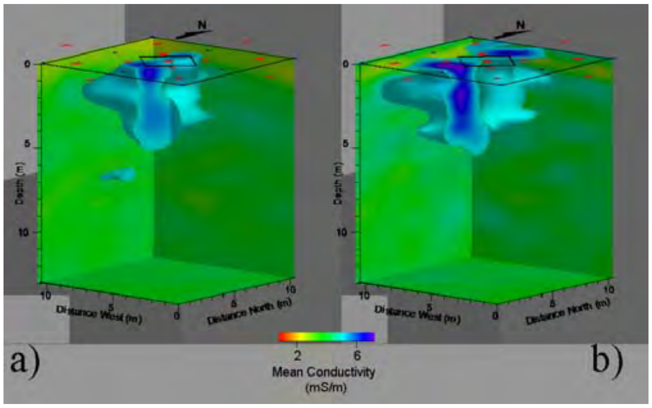

Figure 6-9. **Comparison of Occam's and new inversion method images of STVZ transport data showing (a) image created using the new inversion method and temperature correction, 10/01/01 and (b) image created using Occam's inversion and temperature correction 01/31/02.**

ERT is able to resolve 3D character, form, location and intensity of both infiltrating water fronts and conductive tracer infiltration. Based on the synthetic model studies, some reduction in resolution is apparent. However, bulk conductivity changes appear to be accurately represented in terms of both location and intensity.

This page intentionally left blank.

7. CROSS-BOREHOLE GROUND PENETRATING RADAR

Although XBGPR is used extensively in groundwater investigations (e.g. Hubbard et al., 1997a; Alumbaugh et al., 2000; Binley et al., 2001; LaBrecque et al., 2002; Alumbaugh et al., 2002; Chang et al., 2003a), few efforts have been made to analyze XBGPR resolution and accuracy in a dynamic flow environment. It is important to assess XBGPR image resolution and accuracy because artifacts may be present in the tomograms due to data collection or processing procedures. Kowalsky et al. (2001) simulate the responses of a surface GPR survey using Electromagnetic (EM) forward modeling and compare the GPR reflection cross section with the field outcrops to verify radar information. Day-Lewis et al. (2002) use results from a solute transport simulation to generate synthetic radar data that are then employed to examine a time-lapse inversion algorithm based on the field experiment. Here, a coupled, unsaturated flow and finite-difference (FD) time-domain (TD) EM forward modeling method was used to analyze the resolution of XBGPR images during a series of infiltration experiments similar to that at the STVZ facility. It should be noted that the purpose of this research is not to reproduce the experiments at the STVZ site exactly, but to use the method for examining the resolution of both XBGPR velocity and attenuation tomography, as well as analyzing the results for artifacts that may arise during the data processing.

For initial testing, the XBGPR simulations employed flow simulations from the 2D unsaturated flow code, HYDRUS-2D (Simunek and van Genuchten, 1999) to generate the synthetic moisture fields. During the second round of testing, the XBGPR modeling used results from the high resolution flow simulations performed at SNL as employed in the ERT study described in Section 6. For brevity, a subset of the latter results are presented here.

7.1 Electromagnetic FDTD Forward Modeling

7.1.1 Finite Difference Solutions for Radar Wave Propagation

A staggered-grid finite-difference solution to Maxwell's equations, developed by Holliger and Bergmann (2002), is employed to simulate the EM wave propagation phenomena. Holliger and Bergmann (2002) use the solution, which solves Maxwell's equations in a 2-D cylindrical coordination system, to analyze the response of XBGPR by assuming rotational symmetry with respect to the z-axis. In cross-borehole GPR surveys, transmitter and receiver antennas are placed in two different access boreholes that are assumed to be perpendicular to the surface. Received signals are primarily related to the change in the vertical electric field, and thus the transverse magnetic (TM) mode of Maxwell's equations is employed. The transverse electric (TE) mode is not presented here due to the symmetry of the problem and antenna orientations. In the cylindrical coordinate system, the TM mode form of Maxwell's equations can be represented as follows: (ARE THESE the correct mode equations?)

$$\frac{\partial E_\phi}{\partial t} = \frac{1}{\varepsilon}\left\{\frac{\partial H_r}{\partial z} - \frac{\partial H_z}{\partial r} - \sigma E_\phi\right\}, \tag{7-1}$$

$$\frac{\partial H_r}{\partial t} = \frac{1}{\mu}\left\{\frac{\partial E_\phi}{\partial z}\right\} \tag{7-2}$$

and

$$\frac{\partial H_z}{\partial t} = \frac{1}{\mu}\left\{\frac{1}{r}\frac{\partial\left(rE_\phi\right)}{\partial r}\right\}, \tag{7-3}$$

where ε is the dielectric permittivity, μ is the magnetic permeability, σ is the electric conductivity, t is time, r is the radial distance, z is the depth, and ϕ is the rotation angle about the z-axis in the cylindrical system. E and H represent the electric and magnetic fields, respectively, and subscripts r, z, and ϕ refer to the radial, vertical, and rotational angle components of the electric and magnetic fields.

The TM mode equations can be solved using a staggered finite-different approximation that considers second-order accuracy for both space and time (Yee, 1966; Bergmann et al., 1996):

$$\begin{aligned} E_r^{n+1}(i,k+1/2) = \left\{1+\frac{\Delta t}{2}\frac{\sigma}{\varepsilon}\right\}^{-1} \times \Bigg\{\left[1-\frac{\Delta t}{2}\frac{\sigma}{\varepsilon}\right] E_r^n(i,k+1/2) \\ -\frac{\Delta t}{\varepsilon\Delta z}\times\left[H_\phi^{n+1/2}(i,k+1)-H_\phi^{n+1/2}(i,k)\right]\Bigg\} \end{aligned} \tag{7-4}$$

$$\begin{aligned} E_z^{n+1}(i+1/2,k) = \left\{1+\frac{\Delta t}{2}\frac{\sigma}{\varepsilon}\right\}^{-1} \Bigg\{\left[1-\frac{\Delta t}{2}\frac{\sigma}{\varepsilon}\right]\times E_z^n(i+1,k) - \frac{\Delta t}{(i+1/2)\varepsilon\Delta r} \\ \times\left[(i+1)H_\phi^{n+1/2}(i+1,k)-iH_\phi^{n+1/2}(i,k)\right]\Bigg\} \end{aligned} \tag{7-5}$$

$$\begin{aligned} H_\phi^{n+1/2}(i,k) = H_\phi^{n-1/2}(i,k) + \frac{\Delta t}{\mu}\times\Bigg\{\frac{1}{\Delta r}\left[E_z^n(i+1/2,k)-E_z^n(i-1/2,k)\right] \\ -\frac{1}{\Delta z}\left[E_r^n(i,k+1/2)-E_r^n(i,k-1/2)\right]\Bigg\} \end{aligned} \tag{7-6}$$

where Δr, Δz, and Δt are the discretization intervals with respect to r, z, and t, respectively. Parameters i, k and n are the indices that represent the location of the nodes spatially and temporally within the model.

7.1.2 Model Design for FDTD EM Forward Modeling

To simulate radar wave propagation using the aforementioned approach, the dielectric constant and electrical conductivity must be defined everywhere in space on a Cartesian grid. We define these properties with a petrophysical model that determines soil electrical properties using water saturation and/or soil textures to convert measured water content.

The dielectric constant was estimated by applying equation (7-6 **[?]**) to the volumetric water content that resulted from the unsaturated flow modeling.

$$\theta = 0.0136k_a - 0.033 \tag{7-7}$$

The electrical conductivity was estimated by applying a power-law function that is similar to Archie's empirical equation (Archie, 1942), which describes the relationship between bulk soil conductivity, σ, and the pore water conductivity, σ_w,for saturated soils. In unsaturated soils, Archie's law is written as

$$\sigma = aS^n \phi^m \sigma_w \tag{7-8}$$

where ϕ is the porosity, S is saturation and $a,\ n, m,\ i, k, n$ are constants for a particular soil type (Telford, 1991). Archie's equation assumes that the bulk conductivity is affected by the fluid conductivity, porosity, and saturation. LaBrecque et al. (2002) found that rather than using Archie's law directly, it was better to employ a simpler exponential relationship where the main parameter is residual moisture content, which is in turn dependent on grain size distribution. A single, power-law function was adopted similar to that of LaBrecque et al. (2002). The relationship between bulk conductivity and water content can then be described as

$$\sigma = a \cdot \theta^b \tag{7-9}$$

where σ is the bulk conductivity, θ is the volumetric water content, a and b are the empirical constants that were determined by comparing measured conductivity to neutron-derived water content. Although parameters a and b may vary spatially and are inconsistent through the infiltration experiment (LaBrecque et al., 2002), the same values were used in the EM forward modeling in order to keep a simple, consistent physical relationship between water content and attenuation throughout the water infiltration simulation. Here, $a = 0.11$ and $b = 0.81$ were determined from the XBGPR-estimated water content and the induction logs taken before the infiltration was initiated (Brainard et al., 2002).

Simulations for both freshwater infiltration and a contaminant transport infiltration were completed during this study. Pedotransfer functions for the transport simulations were slightly more complicated than those used to determine electrical properties with the freshwater pulse. For the latter, the contaminant was assumed to be sodium-chloride, and thus increases in salt content in the pore fluid should have no effect on the dielectric constant of the media. However, increases in salt will result in an increase in electrical conductivity of the media. Therefore, the relationship suggested by LaBrecque in equation (6-33) was modified slightly to accommodate an increase in the fluid conductivity. Since Archie's law has the form of

$$\sigma_{bulk} = aS^n \phi^m \sigma_{porewater} \tag{7-10}$$

where pore fluid conductivity is equal to $\sigma_{porewater}$, we can use the relationship suggested by Hall to define pore fluid conductivity based on the concentration of salt in the pore water.

Following this, we can then compute the conductivity of the bulk media by multiplying the STVZ equation used for freshwater by a ratio of the original pore water conductivity at t=0 by the conductivity of the pore water at the current time step being modeled:

$$\sigma = ab\left[\frac{\sigma_{porewater} + \sigma_{salt}}{\sigma_{porewater}}\right]\left(S/m\right) \tag{7-11}$$

The sum in the numerator corrects for times when the plume has not reached the pore space at a given time and resulting in zero conductivity.

XBGPR data were calculated using a Multi-Offset Gathers (MOG's) configuration with data acquisition spacing of 0.25m and a central frequency of 100 MHz. The 12m x 12m x 12m POR-SALSA simulation results were truncated to be two-dimensional panels along the plane y= 0. Each panel computed was 6m in the x direction and 12m in the z direction. Using x=0 as the center of the panel, Three borehole access points were simulated; the first at x=0, the second at x=2.5m and the last at x=-2.5 m. EM simulations were computed for two separate panels for each timestep. The STVZ naming conventions were maintained. The panel defined by Borehole 1 and 2 will be named CINE and the panel defined by 1 and 3 is called CISW. Each panel sampled by 24 transmitters and receivers. The angles of the transmitting antenna to the receiving antenna were limited to 35 degrees as in the field data processing procedures.

Holliger and Bergmann (2002) suggest the criterion

$$c_{\max} \cdot \Delta t \sqrt{\frac{1}{(\Delta r)^2} + \frac{1}{(\Delta z)^2}} \le 1 \tag{7-12}$$

to provide stability of the above finite-difference approximation, where $c_{\max} = \frac{1}{\sqrt{\varepsilon_{\min}\mu_0}}$ is the maximum phase velocity of the EM wave within the model. In order to control the numerical dispersion, Holliger and Bergmann (2002) suggest that a grid spacing with at least 10 grid points per minimum wavelength be required for the FDTD modeling. From the previous XBGPR measurement, a minimum wavelength of 0.89 m was found assuming that the EM wave frequency was at 100 MHz. Therefore, a grid spacing of 0.0625 m by 0.0625 m was chosen for the forward model to stabilize the results. Since grid spacing was given, Δt could be automatically adjusted to stabilize the results using equation (9) in the algorithms. This discretization results in 24,576 cells in each model.

7.2 GPR Tomographic Inversion Algorithm

First-arrival time (travel time) and amplitude of the received EM signals are used as data to invert for velocity and attenuation. For this experiment, the inversion domain consists of a discrete 2D grid of cells that are 0.25m on both sides. The travel time and attenuation for each GPR "time-series" first arrival can be represented as (Sharma, 1997; Jackson & Tweeton, 1996):

$$t_i(or\ \alpha_i) = \sum_{j=1}^{M} p_j d_{ij} \tag{7-13}$$

where $t_i(\alpha_i)$ represents the total travel time or attenuation for the i^{th} ray path, p_j is the average slowness or attenuation of the j^{th} cell, d_{ij} is the distance of the i^{th} ray path within the j^{th} cell, and M represents the number of cells passed through by the i^{th} ray path. The attenuation of each ray path can be calculated as:

$$\alpha_i = -\ln \frac{A_i}{A_0}, \tag{7-14}$$

where A_0 is the amplitude of the transmitted wave form, and A_i is the received amplitude.

Factors other than intrinsic attenuation, including geometrical spreading and the radiation pattern of the transmitter and receiver, also affect the amplitude measured by the GPR system (Peterson, 2001). The transmitting antenna can be thought of as a dipole that radiates EM waves in a spherical geometry. Thus the measured amplitude in a homogeneous medium can be represented as:

$$A_m = A_i(\cos\theta / R), \tag{7-15}$$

where A_i is the amplitude that only depends on the intrinsic attenuation for the i^{th} ray path, θ is the angle measured from the horizontal to the ray path, and R is the distance between the transmitter and receiver antennas.

The inversion code, GeotomCGTM (GeoTom, LLC, 1998), was used to produce images of velocity and attenuation from travel time and normalized amplitude measurements. GeotomCGTM employs a simultaneous iterative reconstruction technique (SIRT) (Jackson & Tweeton, 1996) and ray tracing methods to generate tomographic images. Straight ray inversion, which assumes the ray path between the transmitter and receiver is a straight line, was chosen for both velocity and attenuation inversion.

Theoretically, the first arriving EM wave-fronts tend to travel through high-velocity regions rather than low-velocity regions. This makes the ray paths in an inhomogeneous medium tend to curve around the low-velocity regions and thus they are no longer straight lines. Although it may be more accurate to use curved ray inversion (Alumbaugh et. al, 2002), the difficulty of estimating A0, the correction factor for geometric spreading, and the antenna radiation made the curved ray attenuation inversion difficult to apply. Therefore, straight ray inversion was adopted to generate velocity and attenuation tomograms in this study.

The units for EM wave attenuation employed in this study are neper (Np). The neper is analogous to the decibel (dB), which is used frequently in measuring signal loss and gain ratio, except that the Naperian base (2.718281828….) is used in computing the ratio in nepers rather than the log 10 base. Attenuation in nepers can be converted to decibels by using the equation: 1 neper (Np) = 8.686 dB.

7.3 Potable Water Infiltration Flow Simulations

The freshwater simulations were computed beginning with residual water content in the pore spaces. A two-dimensional slice across the pre-infiltration cube generated by the Sandia flow modeling is shown Figure 7-1. During the actual experiment, the XBGPR data were collected between five boreholes along a single profile. Because the two outer well pairs are not affected by the infiltration experiment, for the XBGPR study we have chosen to simulate only two innermost well pairs which fall within the black rectangle shown in Figure 7-1.

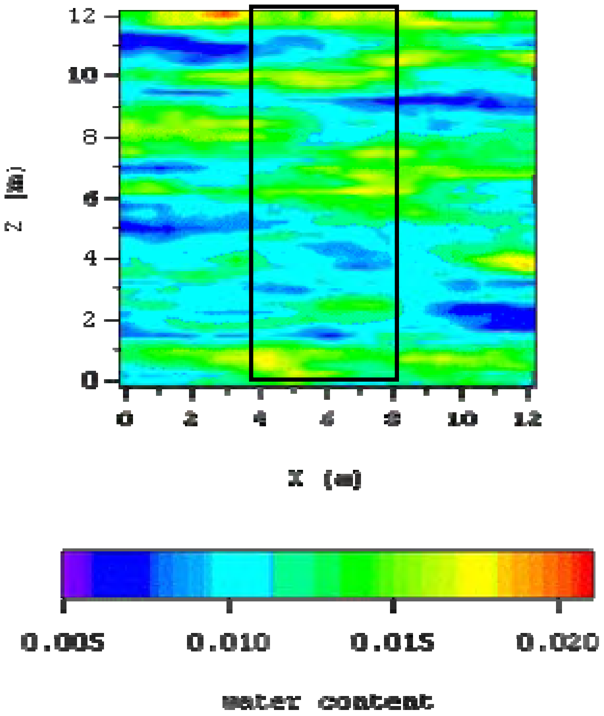

Figure 7-1. Pre-infiltration water content field. The rectangle encloses the area of study.

For the infiltration simulations, potable water was considered to have electrical conductivity of 80 mS/m. The moisture contents that result from inverting the XBGPR pre-infiltration velocity data are given in Figure 7-2. Infiltration simulations were conducted for time-lapses of 10, 20, 30, 60, 90, 180, and 360 days. In Figures 7-3, 7-4, and 7-5 we show the total field moisture content fields and the differences in moisture content over time for times of 10, 30, 60and 60 days after the initialization of infiltration, respectively. Notice that the general trends of the moisture content are recovered. However, the results indicate that a) the image is not able to recover the peak values of moisture content, and b) the images show greater lateral than vertical smearing.

The first point can be explained by the fact that as demonstrated by Alumbaugh et al (2002), XBGPR measurements cannot adequately recover small-isolated zones of high moisture content as these are regions of low velocity The fastest ray path goes around these regions and does not have sensitivity to these zones. This deceased sensitivity for attenuation imaging purposes is due to the angle between a purely horizontal ray path and the ray path at maximum vertical aperture being 35 degrees. This phenomena will tend to limit the horizontal resolution and thus increase the smearing.

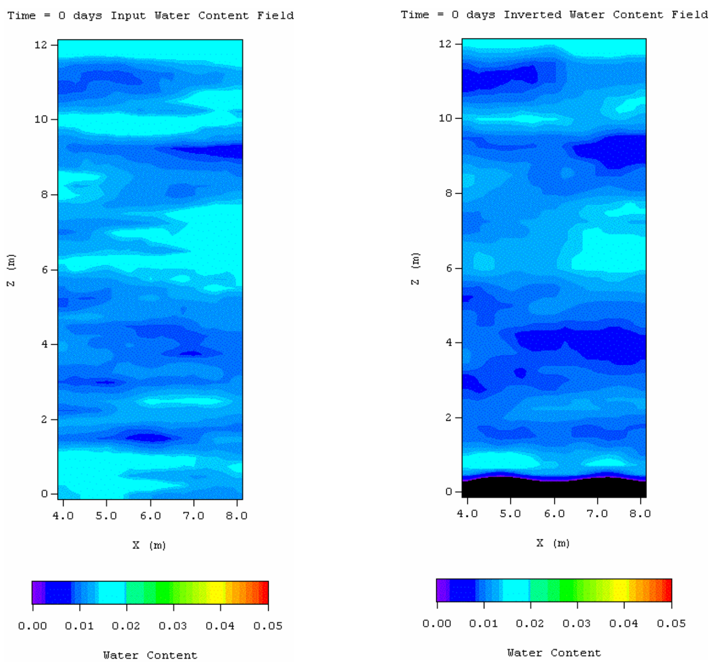

(a) **(b)**

Figure 7-2. **Images of water content at time = Day 0 as estimated from the XBGPR velocity images. (a) The input field, or true model, and (b) the results estimated from the travel-time generated velocity image.**

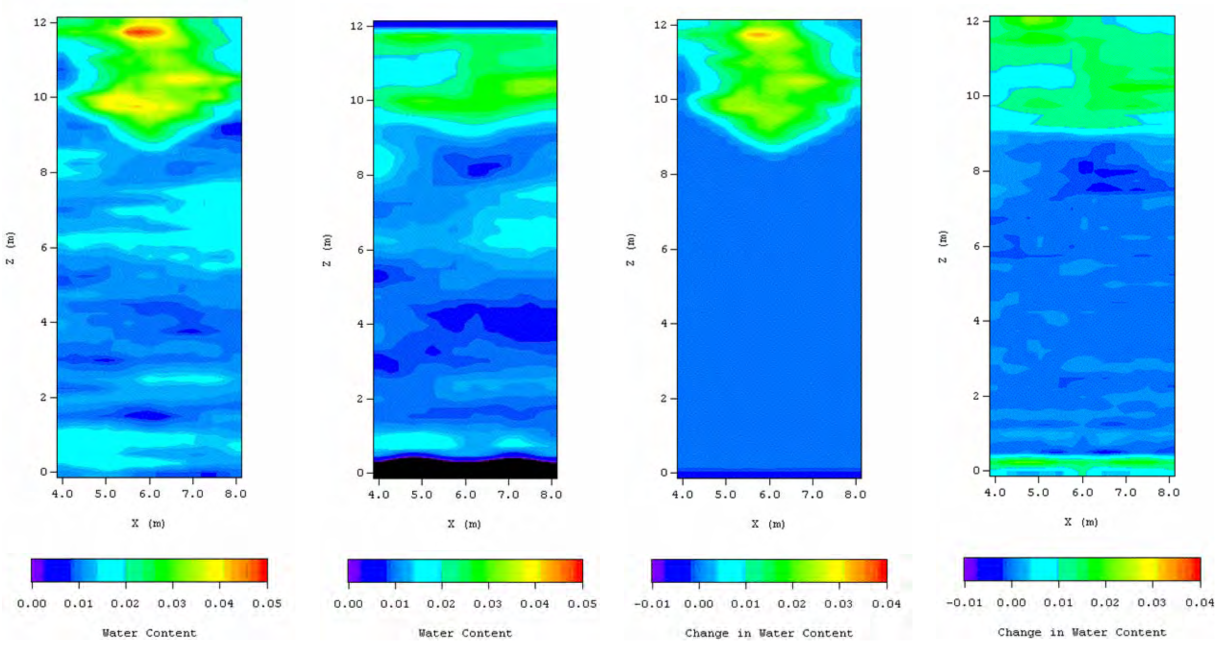

(a) **(b)** **(c)** **(d)**

Figure 7-3. **Images of water content at Day 10 after the beginning of the fresh-water infiltration. (a) The true model total moisture content field. (b) The inversion results in terms of total moisture content. (c) The true-model change in moisture content relative to Figure 7-2a. (d) The inverted change in moisture content relative to Figure 7.2b.**

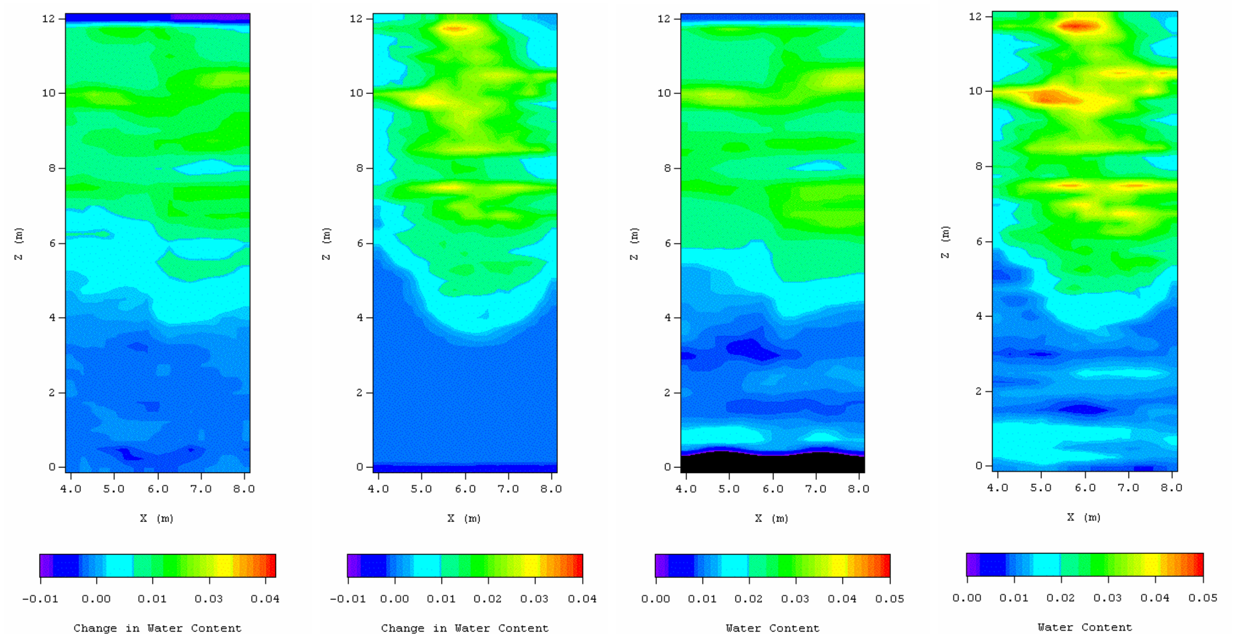

(a) (b) (c) (d)

Figure 7-4. **Images of water content at Day 30 after the beginning of the fresh-water infiltration. (a) The true model total moisture content field. (b) The inversion results in terms of total moisture content. (c) The true-model change in moisture content relative to Figure 7-2a. (d) The inverted change in moisture content relative to Figure 7.2b.**

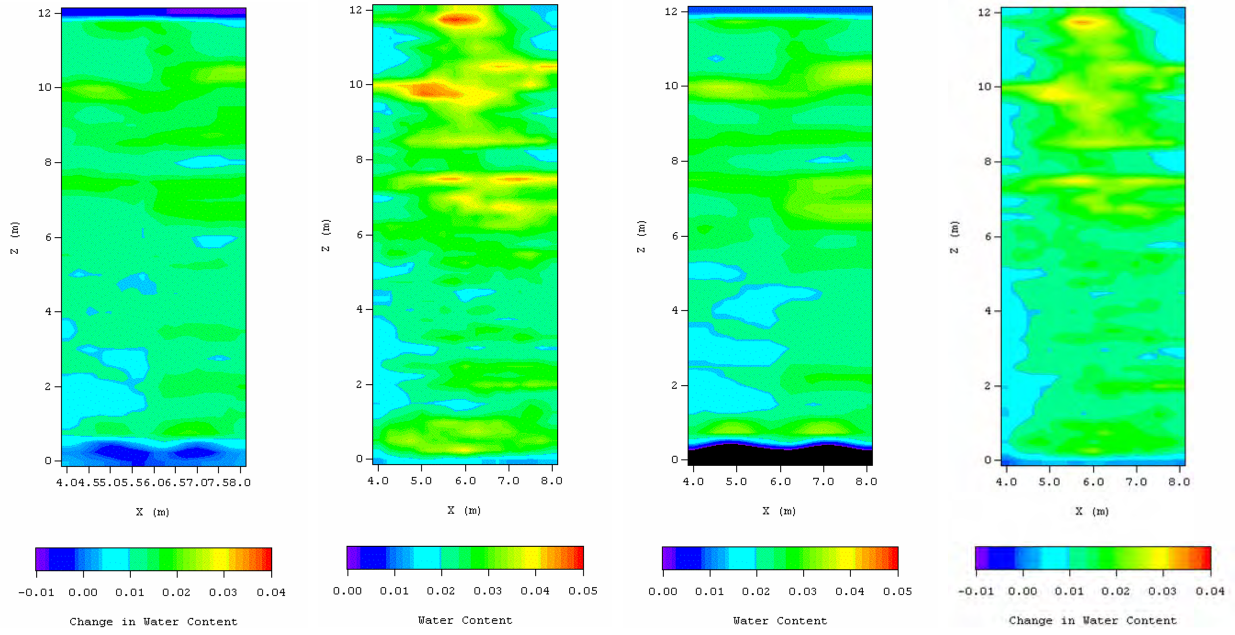

(a) (b) (c) (d)

Figure 7-5. **Images of water content at 60 days after the beginning of the fresh-water infiltration. (a) The true model total moisture content field. (b) The inversion results in terms of total moisture content. (c) The true-model change in moisture content relative to Figure 7-2a. (d) The inverted change in moisture content relative to Figure 7.2b.**

Figure 7-6a shows the pre-infiltration attenuation field and the image resulting from processing and inverting the XBGPR synthesized amplitude data. Note that the image is dominated by diagonal ‘striping’. Similar problems exist in the time-lapse images shown in Figures 7-7 through 7-9. As demonstrated by Chang (2004), these type of artifacts are likely at least partly due to the presence of features which are too small to recover given the sampling interval and frequency used by the system. Additionally, a series of approximations are made during the processing and inversion that violate the physics. For example, the processing and inversion assumes an optical-approximation whereby the source-receiver separations are many wavelengths apart, when in reality they are collected at distances that are only at most one or two wavelengths apart.

Also, the straight ray-path approximation may be invalid for imaging the attenuation, especially during the fresh-water infiltration events when the velocity field, and thus the ray paths, will be changing over time. Artifacts with the same nature were observed by Chang et al (2004) in the analysis of the field data. These numerical experiments prove that the poor images are due to the processing/imaging algorithms rather than data quality therefore.

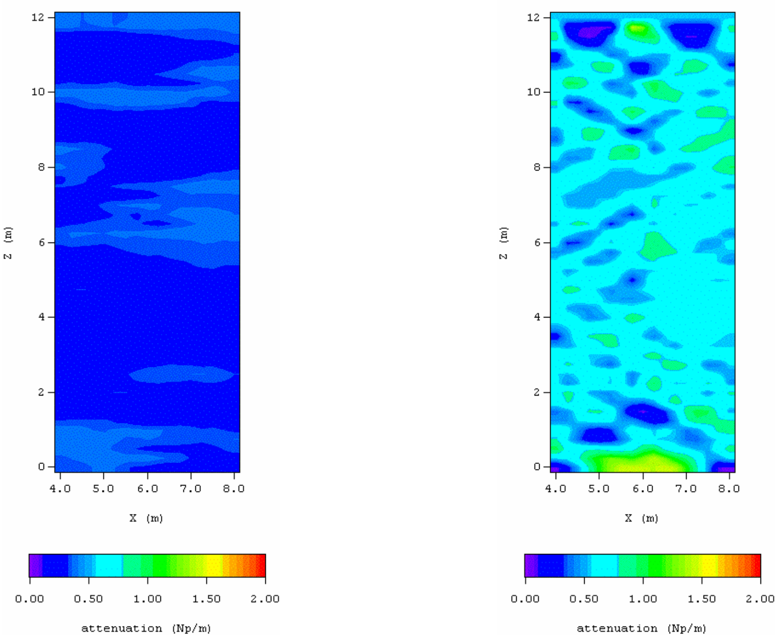

(a) **(b)**

Figure 7-6. Pre-infiltration attenuation field. (a) The input field, or true model, and (b) the results estimated from the attenuation imaging.

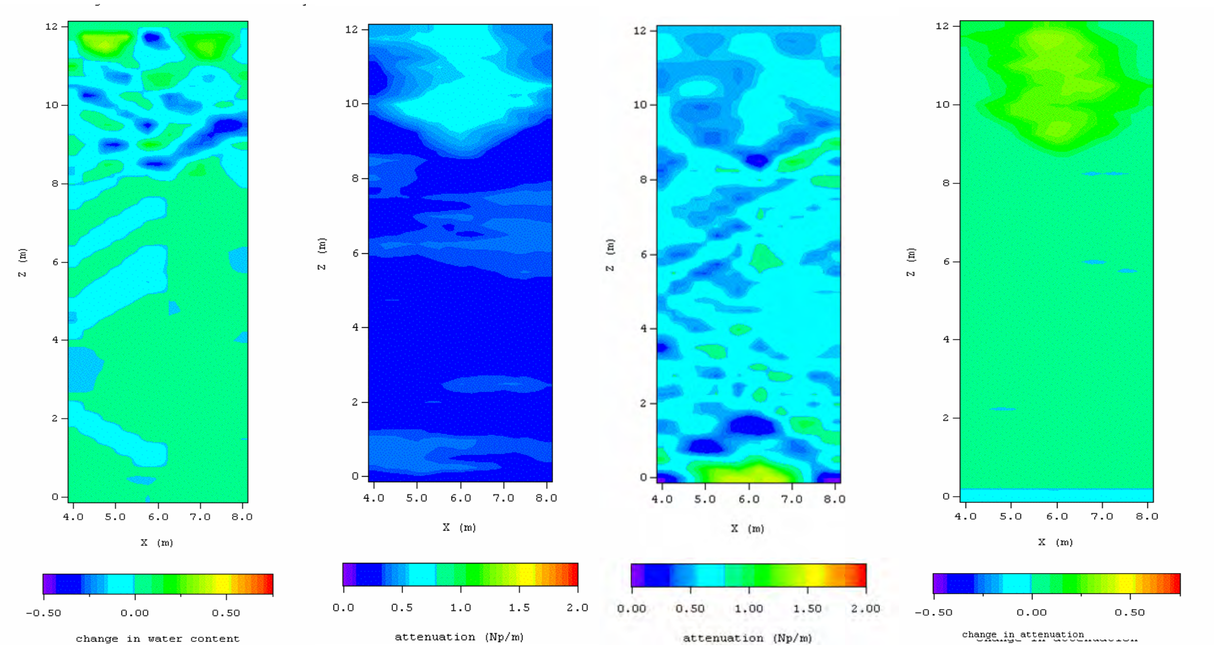

(a) (b) (c) (d)

Figure 7-7. Images of attenuation at Day 10 after the beginning of the fresh-water infiltration. (a) The true model attenuation field. (b) The inversion results in terms of attenuation. (c) The true-model change in attenuation relative to Figure 7-6a. (d) The inverted change in attenuation relative to Figure 7.6b.

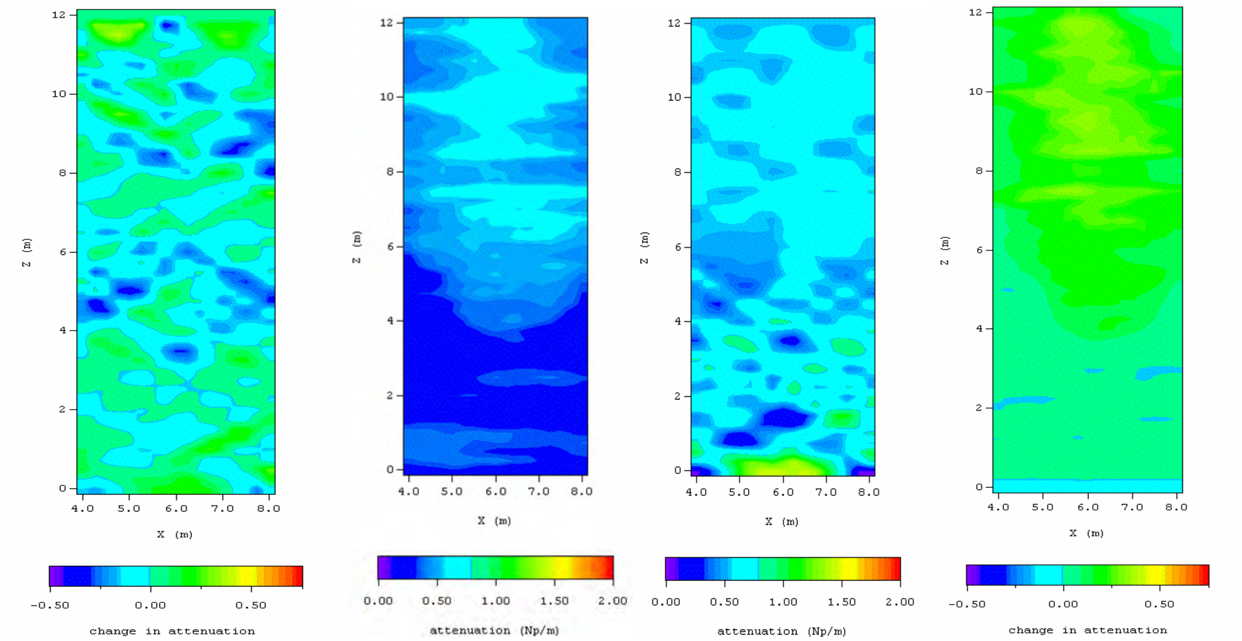

(a) (b) (c) (d)

Figure 7-8. Images of attenuation at Day 30 after the beginning of the fresh-water infiltration. (a) The true model attenuation field. (b) The inversion results in terms of attenuation. (c) The true-model change in attenuation relative to Figure 7-6a. (d) The inverted change in attenuation relative to Figure 7.6b.

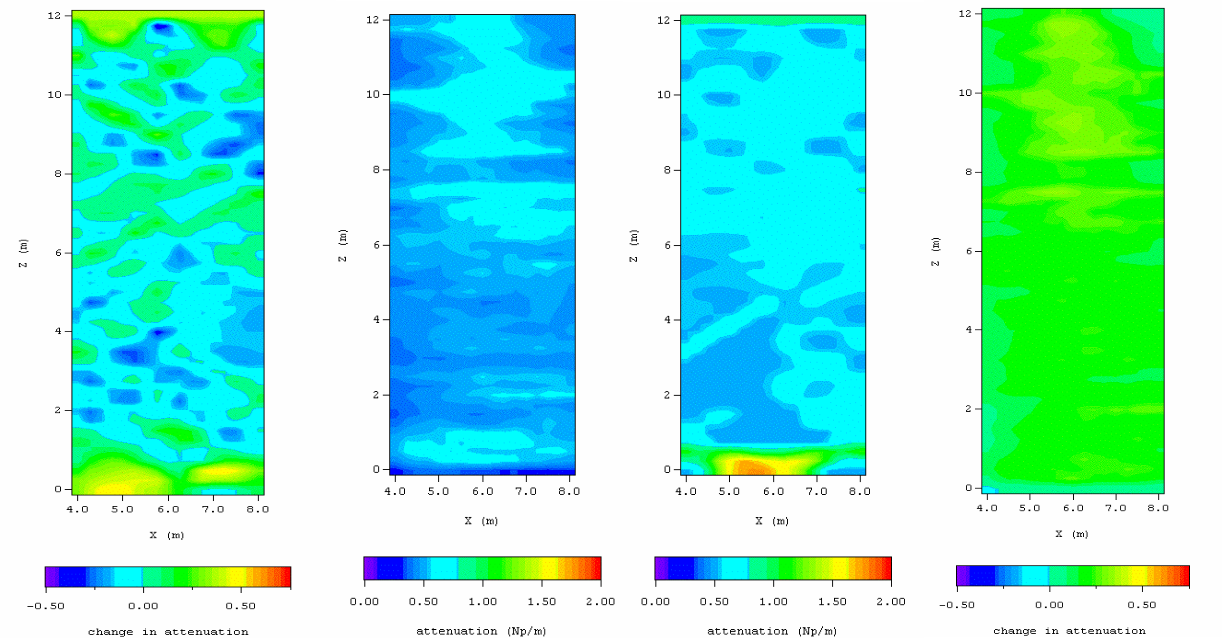

(a) (b) (c) (d)

Figure 7-9. Images of attenuation at Day 60 after the beginning of the fresh-water infiltration. (a) The true model attenuation field. (b) The inversion results in terms of attenuation. (c) The true-model change in attenuation relative to Figure 7-6a. (d) The inverted change in attenuation relative to Figure 7.6b.

7.4 Transport Simulations

Transport simulations were completed for 8 time steps consisting of 0, 10, 20, 30, 60, 90, 180, and 360 days. Time zero days is equal to the end of the freshwater infiltration. Therefore, the water content does not change while salt concentration does, which mimics the actual experiment conducted at the STVZ. This leads to no change in the velocity tomography results during the transport simulation. Therefore, only attenuation images are relevant in this section. Input concentrations of 1000ppm and 6900ppm were computed to mimic the field experiments completed at the STVZ. The results of these simulations are given in Figures 7-10 and 7-11.

Note that the attenuation images of the transport simulation tend to recover the depth of the plume fairly well and that there is a lack of diagonal artifacts observed in earlier images. The lack of artifacts is likely due to the fact that the ray-paths remaining consistent and only the attenuation is changing during these simulations. However, as before, the inversion tends to smear the plume laterally across the distance between the wells. As with the smearing in the velocity images presented in the section above, this is likely due to the small aperture angles employed during the acquisition. In addition, the inversion underestimates the magnitude of the attenuation, more so in the 6900 ppm case in figure 7-11, and in the lower salinity case in Figure 7-10. This is likely caused by a poor representation of the physics in the processing and inversion, both of which tend to favor a small scattering approximation. For these results, a large degree of attenuation is occurring which indicates a larger degree of EM scattering.

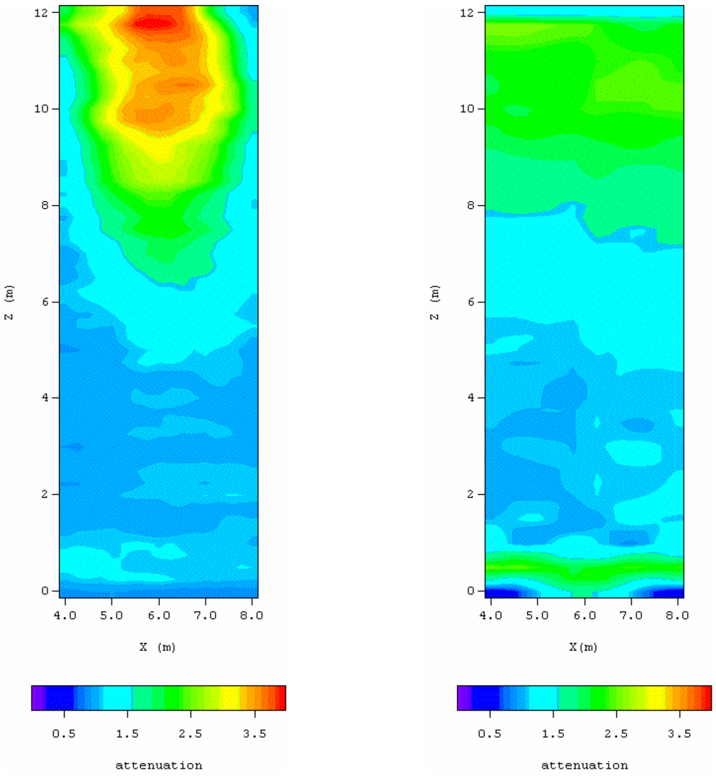

(a) **(b)**

Figure 7-10. Attenuation for 1000ppm transport at time = Day 30. (a) The input attenuation field or 'true model'. (b) The results from processing and inverting the synthesized amplitude data for attenuation.

7.5 Conclusions

The freshwater impulse images reveal several interesting results. First, the velocity images appear to be able to recover features as small as 1m long and 0.25m deep. Second, even though the actual values are slightly subdued in the inverted images, the input fields and the inversion match reasonably well with regard to character and scale. This is not true of the attenuation imaging of the fresh water plume which shows a high degree of diagonal striping which is likely an artifact of the processing and inversion not incorporating the correct physics. With the addition of salt water contamination to the system, the magnitude of the attenuation increased enough that the images are much better than that produced by the freshwater. Again, the overall character of the flow is well constrained. Larger details of the heterogeneous structure are apparent. The input fields and inverted images have similar scales. When the input concentration was increased from 1000ppm to 6900ppm, the depth of transport was clearly imaged in the early time steps. However, when the attenuation exceeded 6 Np/m, most of the signal was lost resulting in a near total loss of resolution at later times.

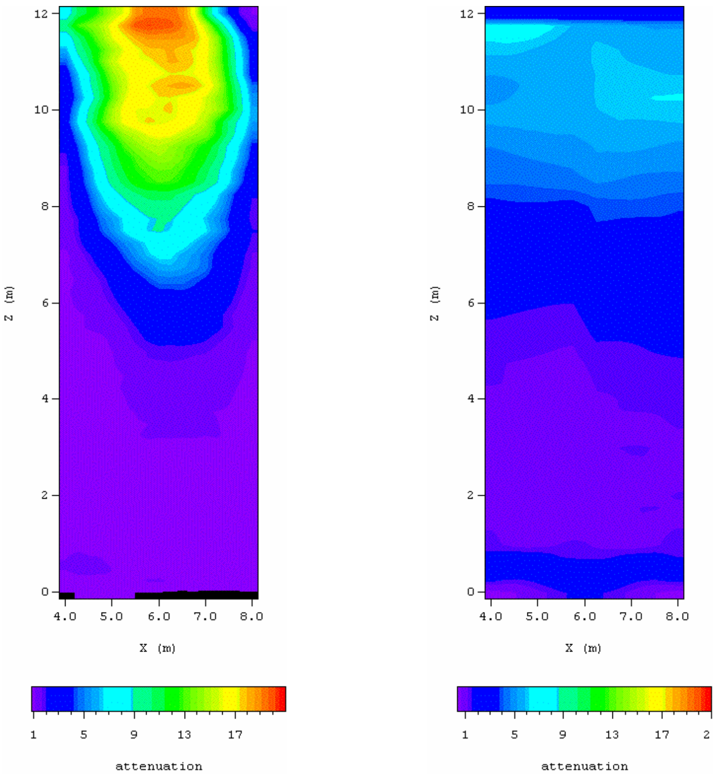

(a) (b)

Figure 7-11. Attenuation for 6900ppm transport at time = Day 30. (a) The input attenuation field or 'true model'. (b) The results from processing and inverting the synthesized amplitude data for attenuation.

This page intentionally left blank.

8. REFERENCES

Altman, S. J., B. W. Arnold, G. E. Barr, C. K. Ho, S. A. McKenna, and R. R. Eaton, 1996, Flow Calculations for Yucca Mountain Groundwater Travel Time (GWTT-95): Sandia National Laboratories/New Mexico SAND96-0189, 170p.

Alumbaugh, D., P. Y. Chang, L. Paprocki, J. R., Brainard, R. J. Glass, and C.A. Rautman, 2002, Estimating moisture contents using cross-borehole ground penetrating radar; a study of accuracy and repeatability in context of an infiltration experiment, Water Resource Research 38 (12), 45-1-45-12.

Alumbaugh, D., L. Paprocki, J. Brainard, and C. Rautman, 2000, Monitoring infiltration within the vadose zone using cross borehole ground penetrating radar, In: Proceedings of the symposium on the Application of geophysics to engineering and environmental problems, pp. 273-281, Environmental and Engineering Geophysical Society. Wheat Ridge, CO, United States.

Annan, A. P., 1996a, Transmission Dispersion and GPR, Journal of Environmental and Engineering Geophysics, 0 (2), 125-136.

Annan, A. P., 1996b, Ground Penetrating Workshop Notes, Sensors & Software Inc., Mississauga, ON, Canada.

Archie, G. E., 1942, Electrical resistivity log as an aid in determining some reservoir characteristics, *Am. Inst. Mining and Metal. (Engr. Transl.)*, 146, 54-62.

Baker, K. E., 2001. Investigation of direct and indirect hydraulic property laboratory characterization methods for heterogeneous alluvial deposits: Application to the Sandia-Tech Vadose Zone Infiltration Test Site. Master’s thesis, Department of Geoscience, New Mexico Institute of Mining and Technology, Socorro.

Bergmann, T., J. O. A. Robertsson, and K. Holliger, 1996, Numerical properties of staggered finite-difference solutions of Maxwell's equations for ground-penetrating radar modeling: Geophysical Research Letters, v. 23, p. 45-48.

Binley, A., P. Winship, R. Middleton, M. Pokar, and J. West, 2001, High-resolution characterization of vadose zone dynamics using cross-borehole radar, Water Resource Research 37 (11), 2639-2652.

Brace, W. F., 1977, “Permeability from resistivity and pore shape”, Journal of Geophysical Research, **82**, pp. 3343-3349.

Brainard, J. R., R. J. Glass, D. L. Alumbaugh, L. Paprocki, D. J. LaBrecque, X. Yang, T.-C. J. Yeh, K. E. Baker, and C. A. Rautman, 2005, The Sandia-Tech Vadose Zone Facility: Experimental design and data report of a constant-flux infiltration experiment. Sandia National Laboratories/New Mexico SAND2005-5070.

Brooks, R. H. and A. T. Corey, 1964, Hydraulic properties of porous media: Fort Collins, CO, Colorado State University.

Burdine, N. T., 1953, Relative permeability calculation from pore-size distribution data, Petrology Transactions, American Institute of Mining Metallurgic Engineering, v. 198, p. 71-78.

Chang, P. Y., D. L. Alumbaugh, J. R. Brainard, and L. Hall, 2003b, Long term monitoring of a two stage salt infiltration experiment using cross borehole GPR (submitted to Journal of Water resources research).

Chang, P. Y., D. L. Alumbaugh, J. R. Brainard, and L. Hall, 2003a, The application of ground penetrating radar attenuation tomography in a vadose zone infiltration experiment, Accepted by Journal of Contaminant Hydrology.

Daily, W. D., A. Ramirez, D. J. LaBrecque, and J. Nitao, 1992, Electrical resistivity tomography of vadose water movement: Water Resources Research, **28**, 1429-1442.

Daily, W. and A. Ramirez, 1999, Electrical imaging of engineered hydraulic barriers; Proceedings of the Symposium on the Application of Geophysics for Environmental and Engineering Problems (SAGEEP) '99, 683-692.

Davis, J. L. and A. P. Annan, 1989, Ground-penetrating radar for high-resolution mapping of soil and rock stratigraphy, Geophys. Prosp., 37, 531-551.

Day-Lewis, F. D., J. M. Harris, and S. M. Gorelick, 2002, Time-lapse inversion of crosswell radar data, *Geophysics*, 67(6), 1740-1752.

Desbarats, A. J., 1995, Upscaling capillary pressure saturation curves in heterogeneous porous media. Water Resource Research, v31, p. 281-288.

Desbarats, A. J., 1997, Geostatistical modeling of unsaturated flow parameters at the Apache Leap Tuff site, *in* Baafi, E.Y. and Schofield, N.A., eds., Geostatistics Wollongong, '96, volume 1: Boston, Kluwer Academic Publishers, p. 621-633.

Deutsch, C. V. and A. G. Journel, 1998, GSLIB Geostatistical software library and user's guide, New York: Oxford University Press, 369 p.

Dey, A. and H. F. Morrison, 1979, Resistivity modeling for arbitrarily shaped three-dimensional structures: Geophysics, 44, 753-780.

Eppstein, M. J., and D. E. Dougherty, 1998, Efficient three-dimensional data inversion: Soil characterization and moisture monitoring from cross-well ground-penetrating radar at a Vermont test site, Water Resource Research 34 (8), 1889-1900.

General Accounting Office, 1998, Understanding of waste migration at Hanford is inadequate for key decisions: GAO Report GAO/RCED-98-80.

GeoTom, LLC., 1998, User Manual for GeotomCG and GeoTom3D, GeoTom, LLC., Apple valley, Minnesota.

Greaves, R., J., D. P. Lesmes, J. M. Lee, and M. N. Toksoz, 1996, Velocity variations and water content estimated from multi-offset, ground penetrating radar, Geophysics, 61 (3), 683-695.

Hall, L.M., 2003, Measuring salinity changes in the vadose zone using downhole electromagnetic induction, [M.S. thesis]: Department of Geoscience, New Mexico Institute of Mining and Technology, Socorro, New Mexico, 259p.

Hawley, J. W., 1983, Geomorphic evolution of Socorro area of Rio Grande Valley. In *New Mexico Geological Society Guidebook*, 34th Field Conference, Socorro Region II, 334.

Holliger, K. and T. Bergmann, 2002, Numerical modeling of borehole georadar data, Geophysics, Vol 67, No. 4, p. 1249-1257.

Hubbard, S. S., Y. Rubin, and E. Majer, 1997a, Ground-penetrating-radar-assisted saturation and permeability estimation in bimodal system, Water Resource Research 33 (5), 971-990.

Isaaks, E. H. and R. M. Srivastava, 1989, An introduction to applied geostatistics, New York: Oxford University Press, 561p.

Jackson, M. J. and D. R. Tweeton, 1996, 3DTOM: Three-dimensional geophysical tomography, Report of investigations 9617, Bureau of Mines, United Stated Department of the Interior., pp. 1-84.

Journel, A. G. and Ch. J. Huijbregts, 1978, Mining Geostatistics, New York,: Academic Press, 600 p.

Keller, G. V. and F. C. Frischknecht, 1966, *Electrical Methods in Geophysical Prospecting*, pp 33-43.

Keller, G. V., 1988, Rock and Mineral Properties. In: M. N. Nabighian (Editor), Electromagnetic methods in applied geophysics, Vol. 1: Theory. Society of Exploration Geophysics, Tulsa, Okla, pp. 13-51.

Knight, R., 1991. Hysteresis in the electrical resistivity of partially saturated sandstones. *Geophysics* 56, no. 12:2139–2147. Mualem, Y., 1976, A new model for predicting the hydraulic conductivity of unsaturated porous media, Water Resources Research, v.12, p 513-522.

Kowalsky M. B., P. Dietrich, G. Teutsch, and Y. Rubin, 2001, Forward modeling of ground-penetrating radar data using digitized outcrop images and multiple scenarios of water saturation, Water Resour. Res., Vol. 37, No.6, p. 1615-1625.

Kunz, K. S. and J. H. Moran, 1958, Some effects of formation anisotropy on resistivity measurements in boreholes: Geophysics, **23**, 770-794.

LaBrecque, D. J. and X. Yang, 2001, Difference inversion of ERT data: a fast inversion method for 3-D in-situ monitoring: Journal of Environmental and Engineering Geophysics, **6**, 83-90.

LaBrecque, D. J., J. Heath G. Bennett, S. Schima, and H. Sowers, 1998, Electrical resistivity tomography for process control in environmental remediation: Proceedings of the Symposium on the Application of Geophysics to Engineering and Environmental Problems, 613-622.

LaBrecque, D. J., M. Miletto, W. Daily, A. Ramirez, and E. Owen, 1996, The effects of noise on Occam's Inversion of resistivity tomography data: Geophysics, **61**, 538-548.

LaBrecque, D. J., G. Morelli, W. Daily A. Ramirez, and P. Lundegard, 1999, Occam's Inversion of 3D ERT data: in: Spies, B., (Ed.), Three-Dimensional Electromagnetics, SEG, Tulsa, 575-590.

LaBrecque, D., D. L. Alumbaugh, Y. Yang, L. Paprocki, and J. Brainard, 2002, Three-dimensional monitoring of vadose zone infiltration using electrical resistivity tomography and cross-borehole ground penetrating radar, Three-dimensional electromagnetics, Methods in Geochemistry and Geophysics, 35, p. 260-272, Elsevier, New York.

LaBrecque, D. J. and D. Casale, 2002, Experience with Anisotropic Inversion for Electrical Resistivity Tomography, Proceedings of the Symposium on the Application of Geophysics to Engineering and Environmental Problems (SAGEEP) ‘02.

Lager, D. L. and R. J. Lytle, 1977, Determining a subsurface electromagnetic profile from high-frequency measurements by applying reconstruction-technique algorithms, Radio Sci., Vol. 12, p.249-260.

Lane, J. W., F. D. Day-Lewis, J. M. Harris, F. P. Haeni, and S. M. Gorelick, 2000, Attenuation-difference radar tomography: Result of multiple-plane experiment at the U.S. Geological Survey Fractured-Rock Research Site, Mirror Lake, New Hampshire, In: Eighth Intl. Conference on Ground Penetrating Radar, Gold Coast, Australia, pp. 666-675.

Luster, G. R., 1985, Raw Materials for Portland Cement: Applications of conditional simulation of coregionalization: Stanford, Calif., Stanford University, PhD. Dissertation, 531p.

Martinez, M. J., P. L. Hopkins, and J. N. Shadid, 1997, LDRD Final Report: Physical Simulation of Nonisothermal Multiphase Multicomponent Flow in Porous Media, Sandia National Laboratories/New Mexico. SAND97-1766.

Martinez, M. J. and P. L. Hopkins, and P. C. Reeves, 2001, POR-SALSA User’s Manual, Sandia National Laboratories/New Mexico. SAND2001-1555.

Morelli, G. and D. J. LaBrecque, 1996, Robust scheme for ERT inverse modeling: European Journal of Environmental and Engineering Geophysics, **2,** 1-14.

Nelson, P.H. and J. R. Hearst, 1985, Well Logging for Physical Properties: McGraw-Hill, 571 p.

Paprocki, L., 2000, Characterization of Vadose Zone In-situ Moisture Content and an Advancing Wetting Front Using Cross-Borehole Ground Penetrating Radar, Master Thesis, New Mexico Institute of Mining and Technology, Socorro, New Mexico, 131 p

Pellerin, L., D. Reichardt, T. Daley, F. Gilbert, S. Hubbard, E. Majer, J. Peterson, W. Daily, and A. Ramirez, 1998, Verification of subsurface barriers using integrated geophysical techniques; Proceedings of the Symposium on the Application of Geophysics for Environmental and Engineering Problems (SAGEEP) ’98, 635-644.

Peterson, J. E., 2001, Pre-inversion Correction and analysis of radar tomographic data, Journal of Environmental & Engineering Geophysics, 6, 1-18.

Ramirez, A., W. Daily D. LaBrecque, E. Owen, and D. Chesnut, 1993, Monitoring an underground steam injection process using electrical resistance tomography: Water Resources Research, **29**, 73-87.

Ramirez, A. L., W. D. Daily, and R. L. Newmark, 1995, Electrical resistance tomography for steam injection monitoring and process control; Journal of Environmental and Engineering Geophysics, **0**, 39-52.

Rautman, C. A. and S. A. McKenna, 1997, Three-Dimensional Hydrological and Thermal Property Models of Yucca Mountain, Nevada. Sandia National Laboratories/New Mexico. SAND97-1730.UC-814.

Rautman, C. A. and S. A. McKenna, 2002, Stochastic Modeling of Fracture Frequency along a Cross-Section at the MIU Site, Tono Region, Japan. Sandia National Laboratories/New Mexico. SAND2002-1395.

Sheets, K. R. and J. M. H. Hendrickx, 1995, Noninvasive soil water content measurement using electromagnetic induction: Water Resour. Res., **31**, 2401-2409.

Slavich, P. G. and G. H. Petterson, 1990, Estimating Average Rootzone Salinity from Electromagnetic Induction (EM-38) Measurements: Aust. J. Soil Res., **28**, 453-463.

Spitzer, K., 1995, A 3-D finite difference algorithm for DC resistivity modeling using conjugate gradient methods: Geophysical J. Int'l, 123, 903-914.

Stubben, M. A. and D. J. LaBrecque, 1998, 3-D ERT inversion to monitor and infiltration experiment: Proceedings of the Symposium on the Application of Geophysics to Engineering and Environmental Problems (SAGEEP)’98, 593-602.

Sullivan and LaBrecque, 1998, Optimization of ERT surveys, Proceedings of the Symposium on the Application of Geophysics to Engineering and Environmental Problems (SAGEEP)’98, 571-581.

Topp, G. C., J. L. Davis, and A. P. Annan, 1980, Electromagnetic determination of soil water content: Measurements in coaxial transmission lines, Water Resource Research 16 (3), 574-582.

van Genuchten, M. T., 1980, A closed-form equation for predicting the hydraulic conductivity of unsaturated soils. *Soil Sci. Soc. Am. J.* 44:892–898.

Yang, X., 1999, Stochastic inversion of 3-d ERT data, Ph. D. dissertation, University of Arizona, Tucson, AZ, 124 p.

Yee, K. S., 1966, Numerical solution of initial boundary value problems involving Maxwell's equations in isotropic media: IEEE Ant. Propag., v. 14, p. 302-307.

DISTRIBUTION:

1	MS 0735	James R. Brainard (6115)
2	MS 9018	Central Technical Files, 8945-1
2	MS 0899	Technical Library, 4414

Sandia National Laboratories